TEKTONIKA

Mesoproterozoic Strike-Slip Faulting within the Åland Rapakivi Batholith, Southwestern Finland

Nicklas Nordbäck *[1,2], **Pietari Skyttä** [2], **Jon Engström** [1], **Nikolas Ovaskainen** [1,2], **Jussi Mattila** [3], **Ismo Aaltonen** [1]

[1]Geological Survey of Finland, Espoo, Finland | [2]Department of Geography and Geology, University of Turku, Turku, Finland | [3]Rock Mechanics Consulting Finland Oy (RMCF), Vantaa, Finland

Abstract Paleostress inversion analysis of outcrop data from brittle fault structures within the Mesoproterozoic 1.58 Ga Åland rapakivi granite, southwestern Finland, revealed two separate strike-slip faulting stages. Stage 1 is dominated by dextral slip along E–W-trending faults under WNW–ESE to NNW–SSE compression, whereas Stage 2 displays less prominent faulting localized in an orthogonal network of N–S and E–W trending faults that developed under NE–SW compression. Relative age constraints indicate that faulting occurred between 1.58 and 0.5 Ga, and further correlation with previously published results indicate a 1.55–1.4 Ga age for Stage 1 faulting, while Stage 2 is compatible with previously described fault reactivations between 1.3–1.2 Ga. To place the results of the fault analyses in a wider framework, we conducted a regional structural interpretation using bathymetric, topographic, and geophysical datasets and reviewed previously published results. Based on the above, we attribute the emplacement of the 1.6–1.5 Ga rapakivi granites and the subsequent development of the Mesoproterozoic sedimentary basins to the reactivation of inherited Paleoproterozoic shear zones during Mesoproterozoic crustal extension. As such, this study contributes towards understanding the relationships between magmatism and strain localisation in continental (failed) rift settings.

Executive Editor:
Craig Magee
Associate Editors:
Laura Federico
Technical Editor:
Bülent Tokay

Reviewers:
Maryam Ezati
N. Harrichhausen

Submitted:
23 June 2023
Accepted:
13 November 2023
Published:
1 February 2024

1 Introduction

Tectonic and gravitational forces within the brittle crust of the Earth causes stresses, which, when exceeding the strength of the rock, lead to brittle failure and the generation of brittle structures, including faults (fault zones and shear fractures) and other fractures (*Marrett and Peacock*, 1999). However, when the stresses affect rock volumes containing structures generated during earlier tectonic events, these pre-existing structures are prone to reactivation (*Sibson*, 1981; *Morris et al.*, 1996). In such a case, the generation of new structures can become localized (*Sornette et al.*, 1993; *Hardacre and Cowie*, 2003), limited, or fully blocked (*Munier and Talbot*, 1993; *Viola et al.*, 2012). Old crystalline terranes have typically undergone multiple tectonic events and, consequently, multiple reactivations (*Viola et al.*, 2009; *Scheiber and Viola*, 2018; *Tartaglia et al.*, 2020), resulting in complex structures in which individual tectonic events can become difficult to trace. Regarding the evolution of the brittle structures in Fennoscandia, multiple tectonic events caused the nucleation of new brittle structures and reactivation of old ones during the period 1.75–1.0 Ga (*Saintot et al.*, 2011; *Viola et al.*, 2013; *Mattila and Viola*, 2014; *Marchesini et al.*, 2019; *Prando et al.*, 2020; *Tillberg et al.*, 2021; *Nordbäck et al.*, 2022). Later tectonic events have been found to merely cause the reactivation of previously formed structures due to the bedrock becoming saturated with brittle structures at around 1.0 Ga (*Munier and Talbot*, 1993; *Mattila and Viola*, 2014). Previous investigations of the post-Svecofennian (i.e. <1.8 Ga) brittle bedrock systems have mainly been associated with the geological characterization of planned sites for nuclear waste disposal, such as at Olkiluoto, southwestern Finland. Studies at Olkiluoto have indicated that the first brittle faults were formed in the brittle-ductile transition zone 1.75 Ga ago (*Marchesini et al.*, 2019; *Prando et al.*, 2020). The next event comprised the nucleation of a new set of faults within a fully brittle environment at around 1.6 Ga, followed by dyke emplacement and the reactivation of pre-existing faults between 1.3–1.2 Ga (*Nordbäck et al.*, 2022), which leaves a relatively long period of 1.6–1.3 Ga without identified fault formation or reactivation.

In this paper, we address the above period of apparent tectonic quiescence by investigating the brittle structures within the 1.58 Ga (*Suominen*, 1991) Åland rapakivi batholith in southwestern Finland (Figure 1), using both field and unmanned aerial vehicle (UAV)-based photogrammetric remote methods (*Bemis et al.*, 2014). With respect to

*✉ nicklas.nordback@gtk.fi

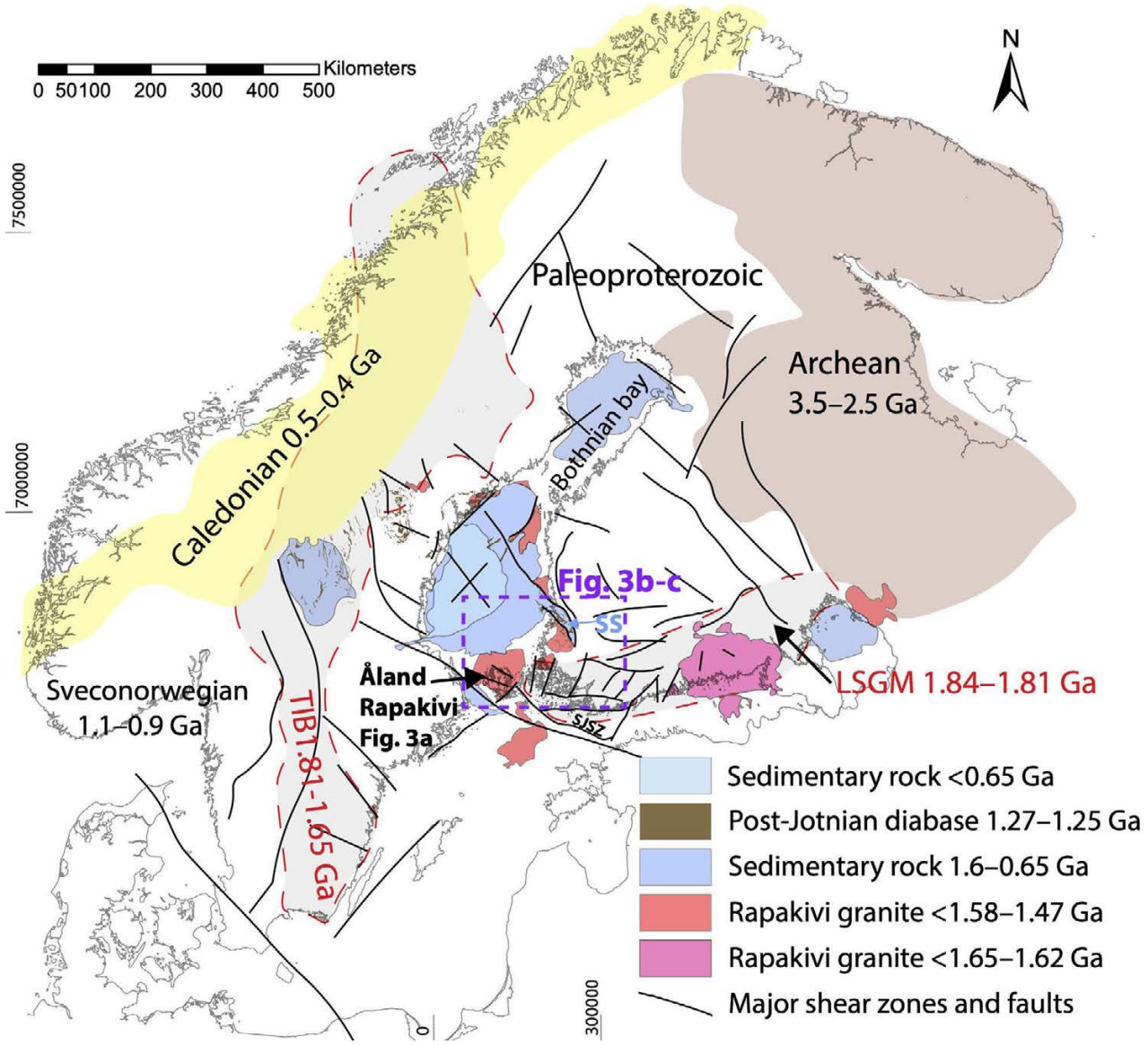

Figure 1 – Major geological provinces and structures of the Fennoscandian shield, including rapakivi granites and other related Mesoproterozoic rock units surrounding the Åland rapakivi batholith. The outline of Figure 3 is indicated on the map. TIB = Transscandinavian Igneous Belt (*Högdahl et al.*, 2004), LSGM = Late Svecofennian Granite-Migmatite zone (*Ehlers et al.*, 1993), SJSZ = Sottunga-Jurmo Shear Zone (*Torvela and Ehlers*, 2010), SS = Satakunta Sandstone (*Kohonen et al.*, 1993). The figure is based on the Geological map of the Fennoscandian shield 1:1,000,000 (*Geological Survey of Finland*, 2001).

brittle investigations and paleostress analysis, the anorogenic and mesoscopically isotropic character of the Åland rapakivi makes it an optimal target for such studies. Based on paleostress inversion analysis (*Marrett and Allmendinger*, 1990; *Angelier*, 1994) of field data associated with discrete sub-vertical faults with limited slip, we recognized two separate deformation stages: likely representing an earlier pure strike-slip and an overprinting strike-slip/transtensional paleostress stage. We further correlate these new results with i) the previously interpreted faulting stages from SE Fennoscandia (*Saintot et al.*, 2011; *Mattila and Viola*, 2014; *Nordbäck et al.*, 2022) and ii) the regional structural geological features and lineaments in southwestern Finland, with specific emphasis on the formation and reactivation of crustal-scale faults. Finally, we discuss the potential implications of these new results for the understanding of the extensional tectonics that led to the (failed) rifting of the Mesoproterozoic crust, including the emplacement of the anorogenic rapakivi granite batholiths (*Rämö and Haapala*, 2005) and deposition of thick red bed continental sandstones during the so-called "Boring Billion" (*Korja et al.*, 2001; *Buntin et al.*, 2019). The results presented in this paper are significant, as they provide a regional insight into the brittle evolution of the crust, which has largely been based on detailed but spatially very limited tectonic studies associated with the planned nuclear waste disposal site characterization in Finland and Sweden (*Saintot et al.*, 2011; *Mattila and Viola*, 2014; *Nordbäck et al.*, 2022).

2 Geological Background

The bedrock of southern Finland is dominated by 1.9–1.8 Ga supracrustal and intrusive rocks that were subjected to high-grade metamorphism and partial melting during the prolonged Svecofennian orogeny (*Nironen*, 1997; *Lahtinen et al.*, 2005, 2009; *Hermansson et al.*, 2008; *Stephens and Bergman*, 2020). Metamorphic peak conditions in southern Finland were reached at 1.82 Ga (*Väisänen and Hölttä*, 1999; *Salminen et al.*, 2022), and the associated penetrative deformation was followed by localized deformation, resulting in a network of crustal-scale shear zones (*Sjöström and Persson*, 2001; *Soesoo et al.*, 2004; *Väisänen and Skyttä*, 2007; *Torvela et al.*, 2008; *Torvela and Kurhila*, 2020). The shear zones are sub-vertical and define a network where the E–W and N–S to NE–SW-trending zones are dominantly associated with dextral strike-slip and dip-slip kinematics, respectively (*Ehlers et al.*, 1993; *Väisänen and Skyttä*, 2007).

The transition from the ductile to the brittle crustal regime in southern Finland occurred at 1.79 Ga, as shown by microstructural, thermobarometric and isotopic studies (*Torvela et al.*, 2008; *Marchesini et al.*, 2019; *Prando et al.*, 2020). Deformation during and immediately after the transition involved brittle reactivation of ductile shear zones due to relaxation of the Svecofennian orogenic stresses (1.79–1.77 Ga; *Väisänen and Skyttä*, 2007) and the generation of the first brittle faults in the Olkiluoto area (*Marchesini et al.*, 2019; *Prando et al.*, 2020) under roughly N–S-oriented compression (*Mattila and Viola*, 2014).

The following 1.65–1.3 Ga period was characterized by crustal thinning and rifting (*Korja et al.*, 2001) and resulted in the formation of a failed rift along the Bothnian Bay (Figure 1). This period started with the emplacement of the anorogenic rapakivi batholiths at 1.65–1.54 Ga (*Rämö and Haapala*, 1995), including the 1.58–1.57 Ga Åland rapakivi batholith (Figure 1; *Suominen*, 1991), which forms the bulk of the bedrock within the present study area, and the roughly coeval swarm of NE–SW-trending diabase dykes occurring southeast of the Åland rapakivi batholith (*Ehlers and Ehlers*, 1977; *Suominen*, 1991). Rapakivi magmatism is post-dated by regionally extensive Mesoproterozoic sedimentary rocks (Figure 1), which were deposited under stable intracontinental conditions (*Kohonen et al.*, 1993; *Pokki et al.*, 2013). The maximum age of the sedimentary deposition and the associated subsidence and faulting is uncertain due to the lack of clastic material from rapakivis or observed cross-cutting relationships (*Kohonen et al.*, 1993). However, a 1.54–1.41 Ga age is suggested by the Ar/Ar ages from the 1.65 Ga (*Vaasjoki*, 1977) Obbnäs rapakivi granite, which *Heeremans et al.* (1996) attributed to resetting of the isotopic system during Mesoproterozoic graben formation or, alternatively, to the cooling of the rapakivi intrusion. According to the model by *Pokki et al.* (2013), initial sedimentation of the Satakunta sandstone (Figure 1) took place during rapakivi magmatism and regional extension, with later normal faulting along bordering NW–SE-trending faults, resulting in a steep and narrow graben. This model is supported by results from *Mattila and Viola* (2014), providing evidence of NE–SW extension based on the kinematics of 1.56–1.37 Ga greisen veins. The minimum age of Mesoproterozoic sedimentary sequences in Fennoscandia is constrained at 1.27–1.25 Ga by cross-cutting post-Jotnian diabase dykes (Figure 1; *Suominen*, 1991).

Recent constraints from paleostress analysis of Olkiluoto brittle structures suggest that transtensional crustal stresses, with approximately NW–SE-oriented compression, could have prevailed before the emplacement of the 1.6 Ga rapakivi granites (*Nordbäck et al.*, 2022). For the actual 1.6–1.3 Ga period of crustal rifting, the few available paleostress constraints are based on conceptual lines of evidence rather than being tied to specific observable structures: emplacement of the rapakivi batholiths is attributed to upward bulging of the mantle under an overall extensional tectonic regime (*Luosto et al.*, 1990; *Haapala and Rämö*, 1992; *Korja and Heikkinen*, 1996; *Nironen*, 1997; *Pajunen et al.*, 2008), with potential structural control by listric shear zones extending to the base of the crust (*Korja and Heikkinen*, 1996), or reactivated subduction-related deformation zones within the lithospheric mantle (*Haapala and Rämö*, 1992; *Rämö and Haapala*, 2005). *Nironen* (1997) correlated the similar E–W and N–S trends of the pre-1.6 Ga and post-1.6 Ga rapakivi intrusions, respectively, and suggested that rapakivi magmatism was not hosted by newly formed faults but instead localized in zones of earlier crustal extension. Contrasting genetic models for the rapakivi magmas also exist: *Vigneresse* (2005) proposed that rapakivi granites were produced due to heat production of the downwelling mantle beneath the Columbia supercontinent, which included a toroidal component that induced strike-slip deformation within the crust. Additionally, *Heeremans et al.* (1996) proposed a genetic relationship between brittle reactivation of shear zones and rapakivi magmatism in a non-extensional regime. Regardless of the tectonic environment, a spatial relationship between the Mesoproterozoic rapakivi granites and particularly the N–S-trending deformation structures is apparent in southwestern Finland (Figure 1).

Emplacement of the post-Jotnian diabases took place approximately synchronously with 1.3–1.2 Ga reactivation of N–S and E–W-striking fault structures in Olkiluoto (*Nordbäck et al.*, 2022), under an overall NE–SW-oriented compression (*Mattila and Viola*, 2014). Subsequent paleostress data are indicative of roughly E–W compression at the onset of the Sveconorwegian orogeny at 1.1 Ga, and E–W extension during orogenic collapse 0.9 Ga ago (*Bingen et al.*, 2008a; *Saintot et al.*, 2011; *Viola et al.*, 2011; *Mattila and Viola*, 2014), which are both associated

with isotopically dated faulting stages in both Finland and Sweden (*Heeremans and Wijbrans*, 1999; *Viola et al.*, 2013; *Tillberg et al.*, 2020, 2021; *Nordbäck et al.*, 2022). The Fennoscandian shield, or at least the Paleoproterozoic parts, reached brittle structural saturation (bedrock became fragmented by brittle structures to a point which hindered the formation of new brittle structures) during the Sveconorwegian orogeny, with later Neoproterozoic deformation merely causing the reactivation of Paleo-Mesoproterozoic structures (*Munier and Talbot*, 1993; *Mattila and Viola*, 2014).

Due to the stable continental setting of the Fennoscandian shield and consequent slow erosion rates, the current erosional level of the basement bedrock is considered to have been reached during Precambrian times (*Kohonen and Rämö*, 2005; *Hall et al.*, 2021). This is supported by the occurrence of Cambrian-aged clastic dykes, for example within the Åland rapakivi (*Bergman et al.*, 1982; *Tynni*, 1982) and Proterozoic granites of southeast Sweden (*Friese et al.*, 2011). Sequences of Paleozoic sediments were later deposited on top of this erosional surface (*Van Balen and Heeremans*, 1998; *Larson et al.*, 1999).

3 Methods and Data

The main body of our data is formed by i) UAV-derived high-resolution orthophotographs, ii) fracture tracelines digitized on these orthophotographs, and by iii) field mapping observations. The well-exposed and relatively continuous bedrock outcrops at Geta, along the northern shores of the Åland Islands (Figure 2A), provide the highest level of detail within our field-datasets, while we used lower-resolution field-data from selected control sites (Figure 3A) to evaluate the i) representativity of the Geta results, and ii) potential variation in paleostress conditions across the Åland batholith. To avoid the pooling of data from different tectonic units (*Sperner and Zweigel*, 2010) and to identify possible local variations within the mapped area of Geta, the Geta outcrop area was divided into five subregions (Figure 2A), in which we performed separate analyses of the respective data. The size of the subregions was chosen based on data availability so that consistent-sized datasets were achieved for each region. Furthermore, to place the results into a regional context, we also mapped lineaments from within the region of southwestern Finland (Figure 3).

3.1 Remote Mapping

3.1.1 Lineament Interpretation

Lineament interpretation can be used for mapping linear topographic and geophysical anomalies (*O'Leary et al.*, 1976; *Nordbäck et al.*, 2023), which can be used as a proxy for brittle structures. However, without actual confirmatory studies, they should be considered as unspecified zones of discontinuities in the bedrock that, in Finland, resulted from selective glacial erosion associated with intense bedrock fracturing (*Krabbendam and Bradwell*, 2014; *Skyttä et al.*, 2015, 2023).

We used the major lineaments from the 1:200,000 integrated lineament interpretation by *Ovaskainen et al.* (2023), which we further extended to cover all the onshore areas of the Åland main islands (Figure 3A: Åland, Föglö). The integrated interpretation is based on airborne topographic LiDAR-data (Light Detection and Ranging; *Abdullah et al.*, 2013; *Soliman and Han*, 2019) produced by the *National Land Survey of Finland* (2019, with 0.5 points/m^2 and a mean altitude error of 0.3 m) and the airborne magnetic (Mag) and electromagnetic (EM) datasets of the Geological Survey of Finland (collected from an altitude of 30 m, with a line spacing of 200 m; *Hauta-niemi et al.*, 2005; *Geological Survey of Finland*, 2007a,b). For more details on geophysical lineament interpretation, see Nordbäck et al. 2023 and references therein. For the surrounding region of southwestern Finland (Figure 3B), we mapped the elongated depressions within the submerged offshore areas from bathymetric data (EMODnet Bathymetry Consortium, 2018) and correlated the resulting structural network with the deformation zones recognized from aeromagnetic data ((Figure 3C); Hautaniemi et al., 2005). This bathymetric/aeromagnetic interpretation is an update and an extension of the work of *Väisänen and Skyttä* (2007) and *Torvela et al.* (2008) and provides improved coverage between the SW coast of Finland and Åland Islands. In this study, we compared the onshore lineament pattern from the Åland main islands with the faults investigated in this paper, as well as with the regional network of structural discontinuities within the surrounding region of southwestern Finland. All source datasets are presented in Supporting Information (Appendix A).

3.1.2 UAV Mapping

For outcrop investigations, we used remote mapping of photographic UAV datasets. We complemented a previously published UAV-orthomosaic image dataset from the Getaberget outcrop (Figure 2; *Nordbäck and Ovaskainen*, 2022) with additional outcrop orthomosaics acquired from other control sites of the Åland archipelago (Boxö, Vårdö, Föglö and Eckerö), using the methods and equipment described by *Ovaskainen et al.* (2022). All used orthomosaics have an average ground sampling distance of 0.55 cm/pixel.

Prior to the field mapping of the Geta outcrop area, we digitized fracture traces as 2D polylines based on orthomosaics (Figure 2) following topological recommendations by *Nyberg et al.* (2018). We had access to the fracture dataset of *Ovaskainen et al.* (2022), which contains fractures digitized from systematically placed circular target areas with diameters up to 50 m. To find additional kinematic structures outside the target areas and to

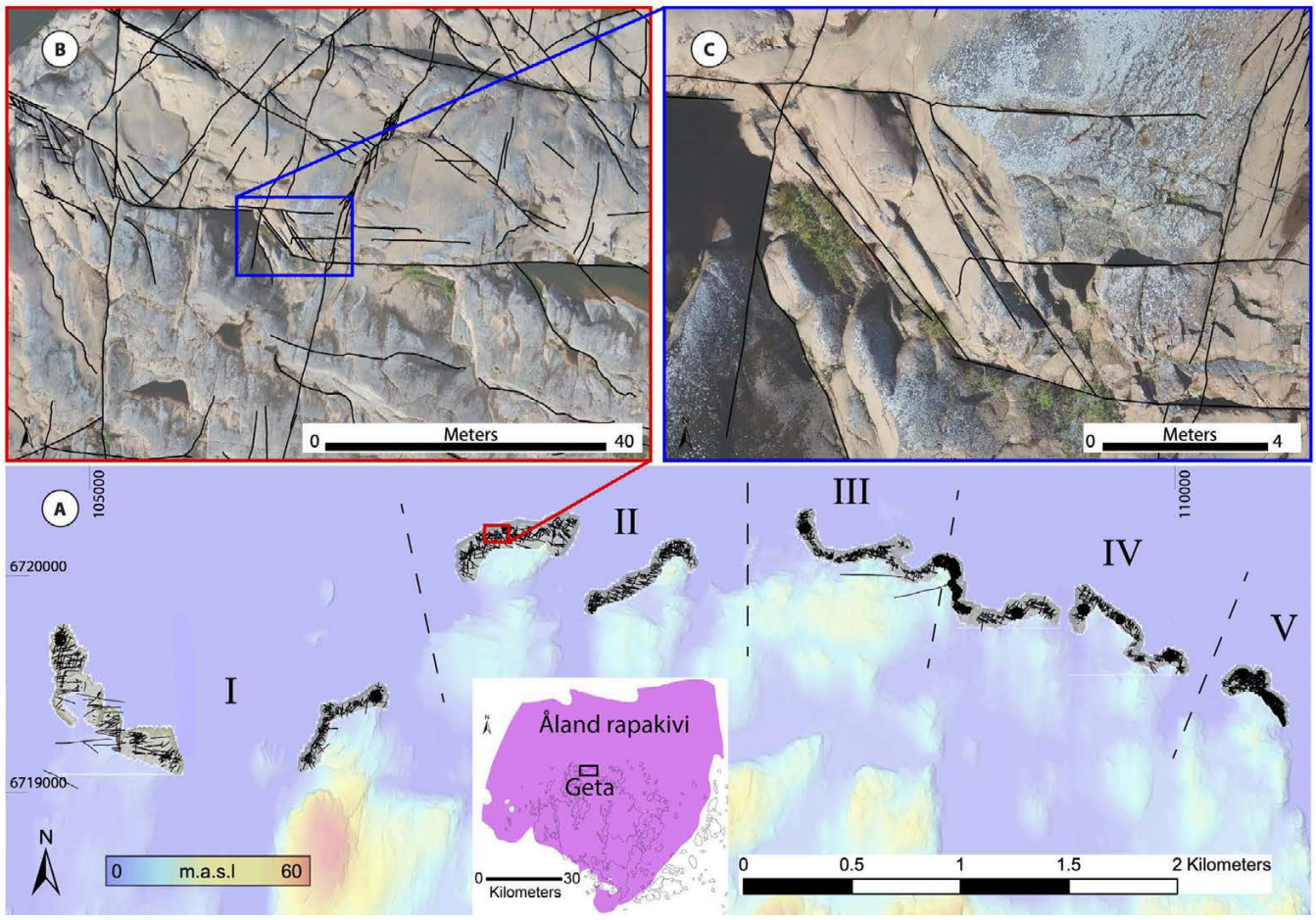

Figure 2 – A) UAV data from the Geta outcrop area on top of a LIDAR DEM (the location of the Geta outcrop area is indicated on the inset map, covering the Åland rapakivi batholith). Subregions I–V are numbered and indicated with dashed lines. Digitized fracture traces are visualized as black lines. **B–C)** Zoom-ins to one of the outcrops within subregion II, displaying the resolution of orthomosaics and level of detail of fracture trace mapping.

map all long fractures (>20 m), we complemented the dataset by digitizing most of the remaining long fractures and all remotely detectable potential faults (regardless of the length). Based on the orthomosaics, we classified specific fractures as shear structures by recognizing their systematic geometrical and topological relationships with the shorter abutting fractures. These potential shear structures were used to guide the subsequent field work. Finally, we digitized a representative set of shorter fracture traces to have better spatial coverage of the main fracture sets. The dataset resulted in a total of 43,701 fracture traces (21,681 from *Ovaskainen et al.*, 2022, and 22,020 new ones).

3.2 Field Mapping

We conducted field mapping using the orthomosaics to locate and verify the traces of remotely mapped potential shear structures, and to gather a representative sample of field data from all fracture types. For each investigated fracture trace, we registered the fracture type according to the glossary by *Peacock et al.* (2016) and measured the dip and dip direction of the fracture plane. We use the term fracture to collectively refer to all unspecified brittle discontinuities within the bedrock. For the sake of simplification, in this paper, we refer to all brittle structures of shear failure (shear fractures and fault zones) as faults. Joints are individual mode I fractures that lack macroscopically observable indicators of movement between the fracture surfaces, and with tension fracture, we refer to any syn-fault fracture that we interpret to be kinematically linked to a fault or shear fracture. Fault zones are typically larger brittle structures, with a distinct fault core (or cores) and damage zone, which have accommodated more deformation compared to isolated shear fractures and are composed of a network of shear fractures and other kinematically related fractures. Thus, the structures we classify as shear fractures lack significant core zones.

For all mapped faults, we collected detailed parameters, including kinematics, uncertainty of kinematics, field observable fault length, fault type (shear fracture, fault zone), filling and alteration. When applicable, we measured the orientation of slip lineation, displacement, core type (according to the classification by *Sibson*, 1977), core width, and damage zone width. In addition, some fracture traces and faults were added or modified during field work and afterwards updated in the digital fracture trace dataset.

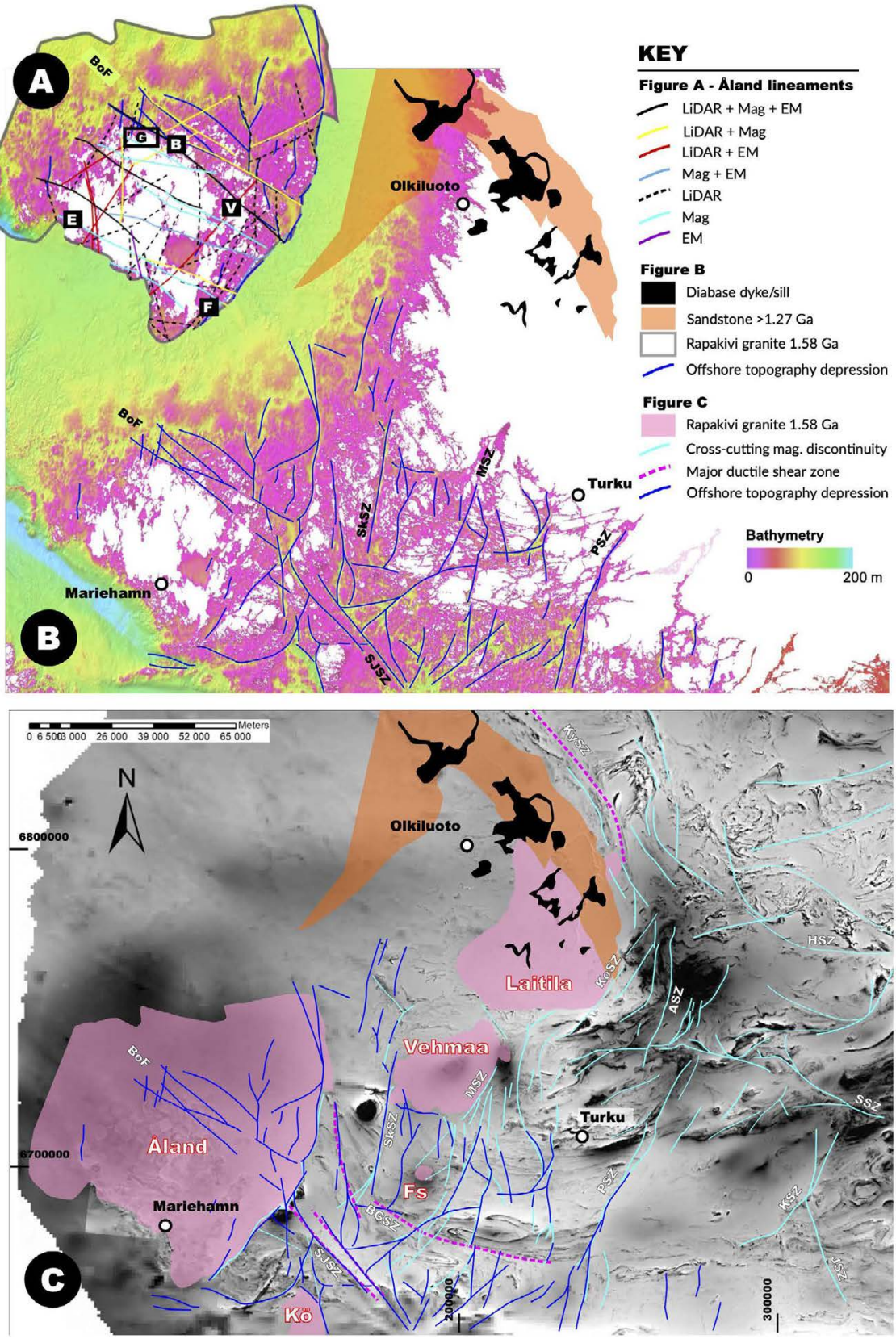

Figure 3 – Review of the structural discontinuities within the southwestern Finland area. **A)** Structural discontinuities within the Åland rapakivi batholith (modified from *Ovaskainen et al.*, 2023) and the sub-areas of this study. B = Boxö, E = Eckerö, F = Föglö, G = Geta, V = Vårdö. BoF = Boxö Fault. **B)** Distinct elongate depressions within the onshore areas as recognized from the bathymetric data (*EMODnet*, 2018). MSZ = Mynälahti Shear Zone, PSZ = Paimio Shear Zone, SJSZ = Sottunga-Jurmo Shear Zone, SkSZ = Skiftet Shear Zone. **C)** Interpretation of the semi-brittle to ductile shear zones (light blue) from aeromagnetic data (*Geological Survey of Finland*, 2007a) and comparison with the structural lines from the bathymetric data (Figure B) in the offshore area. BGSZ = Björkö-Gullkrona Shear Zone, HSZ = Hämeenlinnna Shear Zone, JSZ = Jyly Shear Zone, KSZ = Kisko Shear Zone, KoSZ = Kolinummi Shear Zone, KySZ = Kynsikangas Shear Zone, SSZ = Somero Shear Zone. Rapakivi intrusions: Fs = Fjällskär, Kö = Kökar (*Suominen*, 1991; *Geological Survey of Finland*, 2001; *Väisänen and Skyttä*, 2007; *Torvela et al.*, 2008; *Kraatz*, 2013; *Pitkälä*, 2019; *Ovaskainen et al.*, 2023).

Since fault structures are commonly composed of several individual fracture traces, their descriptive attribute data were collected as a point dataset, while the data collected for individual polylines only describe individual fracture traces. All classifications and mapping data were stored as attribute information in an ArcGIS (© ESRI) geodatabase.

Our field data from Geta include orientation information from about 500 mapped joints, 160 mapped fault planes, and 115 mapped tension fractures associated with faults or shear fractures. To provide a regional correlation, in addition to the more comprehensive dataset of brittle fractures from Geta, we also included fault kinematic data from smaller and more scattered outcrops within the areas of Boxö, Vårdö, Föglö, and Eckerö (Figure 3A).

3.3 Paleostress Analysis

In an ideal mechanically isotropic material, the slip on a fault plane occurs parallel to the maximum resolved shear stress, constituting the so-called Wallace-Bott hypothesis (*Bott*, 1959; *Wallace*, 1951). Assuming such conditions, fault-slip data can be used for paleostress inversion analysis (*Angelier*, 1994; *Lacombe*, 2012; *Pascal*, 2021). The studied Åland rapakivi batholith shows some compositional and textural heterogeneity (*Laitakari et al.*, 1996), while the mesoscopic texture is isotropic. In addition, the anorogenic character and Mesoproterozoic age of the rock limits the quantity of mechanical anisotropies (i.e. Paleoproterozoic ductile and brittle structures), and as such, the oldest brittle structures that formed within the rapakivi can be assumed to have formed in mesoscopically isotropic material.

By utilizing kinematic datasets and stress inversion algorithms, the directions of principal stresses an be calculated, along with the relative magnitudes of the principal stresses, in the form of the stress ratio R (σ_2 - σ_3 / σ_1 - σ_3). For more information on the mathematical basis for calculating principal stress tensors, see e.g., *Angelier* (1979, 1984), *Žalohar and Vrabec* (2007) and *Ezati et al.* (2020). Stress regimes are determined by the nature of the vertical principal stress tensor: i) extensional when σ_1 is vertical, ii) strike-slip when σ_2 is vertical, and iii) compressional when σ_3 is vertical. Stress regimes can be described by the modified stress regime index R′, derived from the stress ratio R (*Delvaux et al.*, 1997). When σ_1 is vertical, R′ = R, when σ_2 is vertical, R′ = 2 – R, and when σ_3 is vertical, R′ = 2 + R. Depending on the stress ratio, the character of the stress regime may vary and, for example, for strike-slip stress regimes (vertical σ_2), a pure strike-slip stress tensor will have an R-value of 0.5, while R-values above 0.75 indicate a transtensive stress tensor and values below 0.25 indicate transpression (*Delvaux et al.*, 1997).

Typically, fault-slip indicators used for paleostress inversion analysis include information on the orientation of the fault plane, the orientation of the slip line (e.g., striation on a slickenside surface; Figure 4A), and the sense of movement, which are in combination referred to as the fault-slip datum (*Marrett and Allmendinger*, 1990). Within the area of the present study, which is characterized by intense glacial erosion and mostly 2D outcrops, we had very limited access to full fault-slip data. For this reason, we used slip planes and the tension fractures kinematically associated with the faults (*Delvaux and Sperner*, 2003; *Blenkinsop*, 2006; *Healy et al.*, 2006) as the primary dataset for the paleostress analysis. These tension fractures represent en échelon fractures formed perpendicular to the minimum compressive stress during the initial stages of faulting (*Scholz*, 2007). Strongly sigmoidal en échelon features were not observed within the Åland rapakivi, which indicates that no significant rotation of stress or fractures occurred during shearing. However, when slight curvature at e.g., tips of en échelon fractures was observed, we measured the orientation of the planar part of such fractures. When available, we used fault-slip data over the tension fractures to reduce uncertainty, as tension fractures may in some cases be difficult to distinguish from joints.

The studied fault structures are of varying orientation and kinematics but share similarities regarding fracture type, morphology, and mineral filling. Regarding mineral fillings, it is also difficult to observe fillings or thin coatings from the eroded bedrock outcrops we have studied. Thereby, field classification into fault families could only be performed based on the orientation and kinematics of the faults.

In the analysis of our datasets, we followed the same workflow for paleostress inversion as described by *Mattila and Viola* (2014) and *Hestnes et al.* (2022), using 'WinTensor' software (*Delvaux and Sperner*, 2003). For a rough sorting of the fault-slip data into sub-sets, we first used the right dihedron method, followed by the iterative method of "rotational optimization" to find the optimal stress tensor for each analyzed sub-set. During the rotational optimization stage, data with a misfit angle >30° between the observed slip direction and the theoretical slip direction (based on the produced stress tensor) were deemed incompatible and removed from the sub-sets, and either assigned to another sub-set or rejected from further analysis.

Our kinematic dataset from the Geta outcrop area includes a total of 139 observations. In the paleostress analysis stage, slip lineation observations with an angular field measurement error greater than 20° between the lineation and fault plane were omitted from further analysis. Lineations with angular errors of less than 200° were projected to the fault plane. For observations consisting of the fault plane and tension fracture, WinTensor software accepts angular differences between 15–60° for the fault plane and tension fracture, and we

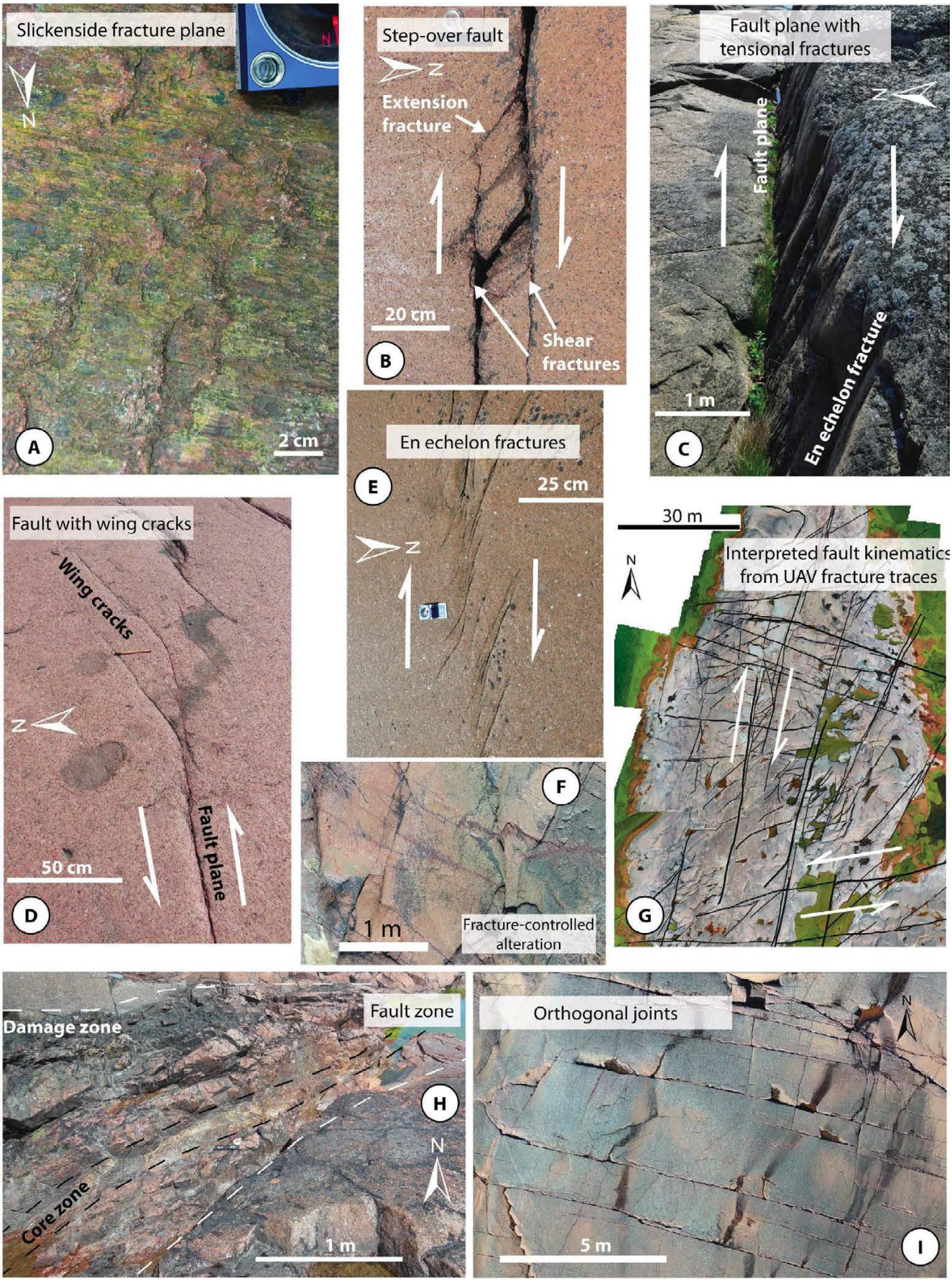

Figure 4 – Examples of brittle structures from Geta. **A)** Slickenside fractures surface. **B)** Dextral step-over fault. **C)** Fault plane with kinematically related tension fractures (indicating dextral sense of movement). **D)** Fault plane with sinistral wing cracks. **E)** Dextral en échelon fractures. **F)** Reddish alteration halo around fracture planes. **G)** UAV fracture traces indicating kinematics of long shear fractures. **H)** Fault zone including a core of incohesive fault rock and an enveloping damage zone of intensively fractured rock. **I)** Orthogonal arrangement of joints.

therefore also removed observations not fitting these criteria. A total of 21 fault kinematic observations were omitted and 118 were accepted for further analysis, consisting of 105 shear planes with tension fractures and 13 slip lineation measurements. The complementing regional survey, covering other control sites of the Åland archipelago, included 50 additional observations of shear planes and associated tension fractures, and 13 fault slip measurements. The WinTensor software also estimates the quality of the resolved stress tensors (from A to E), which is based on factors such as number of data, slip deviation, slip sense confidence for individual faults, and type of data (*Delvaux and Sperner*, 2003).

Since joints propagate perpendicular to the minimum principal stress (σ_3) and since variations in the orientation of the maximum principal stress can be assumed to be lower compared to the two other principal stress orientations, joint data can reveal information about the paleostress conditions during joint formation (*Dyer*, 1988; *Baer et al.*, 1994). Thus, depending on the clustering of three-dimensional joint orientation data, information on the orientation of all principal stress orientations can be gained. To acquire information on the paleostress during the formation of joint sets on Geta, we used GArcmB software *Yamaji* (2016), which adopts an automated code for searching for the best fit with mixed Bingham distributions (*Jolly and Sanderson*, 1997; *McKeagney et al.*, 2004). GArcmB estimates both the orientation of principal stress axes and stress ratio (R) for each joint set based on the Bingham concentration parameters K_1 and K_2 (*Bingham*, 1974; *Yamaji et al.*, 2010). The spread of orientations from the minimum to maximum concentration axes is described by K_1 and from the maximum to intermediate by K_2. For circular distributions the value of $K_1 = K_2$, for elliptical ones $K_1 < K_2$ and for girdle distributions $K_1 \ll K_2$.

4 Results

4.1 Lineaments

The pattern of lineaments within the onshore parts of Åland is dominated by a set of spaced but penetrative, >20-km-long NW–SE trending lineaments that can be recognized from all datasets (LiDAR, Mag, EM, and Bathymetry; Figure 3A). The most distinct lineament is the Boxö Fault (BoF; *Kraatz*, 2022), which bounds the NE margin of the Åland main island. This major lineament has a length exceeding 60 km and is evident in all datasets. Roughly N–S-trending linear features are present in LiDAR and EM data, particularly in the western part of the Åland Island, as well as in the LiDAR data scattered across the island. The central onshore areas mainly display NE–SW-trending LiDAR-based lineaments and a few LIDAR + EM lineaments, which are not supported by magnetic data. The N–S and NE–SW-trending lineaments are shorter than, and frequently show an abutting relationship with the dominant NW–SE lineaments.

The eastern contact of the Åland rapakivi batholith stands out in the bathymetric data as a narrow curvilinear NE–SW to N–S-trending depression, which extends over 100 km in length (Figure 3B). Another distinct but isolated feature is the NW–SE-trending zone terminating against the SE contact of the Åland batholith (SJSZ). This feature comprises two straight and narrow depressions, which terminate against the rapakivi batholith and have a minimum length of 50 km. At the rapakivi contact, this lineament makes a right-lateral step and continues as a wider zone of parallel bathymetric lineaments (BoF), which are, however, not equally distinct and continuous (Figure 3B).

Distinct narrow and elongate N–S to NNE–SSW depressions display a systematic spaced pattern extending beyond the Turku area in the east to the eastern contact of the Åland batholith in the west (Figure 3B). The above lineaments correlate spatially with the elongated straits between the islands in the archipelago and with the bays extending into the mainland of Finland. Most of the N–S to NNE–SSW lineaments terminate against the major NW–SE lineaments, dominantly outside the rapakivi batholiths, but locally also within them, such as north of the BoF.

The linear features within the aeromagnetic map over the southwestern Finland mainland and archipelago (Figure 3C) are either major zones of pronounced banding associated with ductile deflections (e.g., SJSZ), or more discrete discontinuities that cross-cut the banding within the supracrustal rocks or delineate the occurrence of supracrustal and (magnetically homogeneous) intrusive rocks. With respect to their orientation, these structures roughly fall into N–S and E–W-trending categories. The largest zones with significant ductile transposition but with no cross-cutting features comprise the NNW-trending Kynsikangas SZ (KySZ) in the north and the NW–SE-trending SJZS in the south. Another major E–W zone, the Hämeenlinna SZ (HSZ), deflects towards NW in the west and terminates before making contact with the KySZ. Like the HSZ, the E–W-trending Somero SZ (SSZ) is cut by the N–S features, as it is segmented by a set of spaced but penetrative shear zones within the area bound by the Paimio (PSZ) and Skiftet Shear zones (SkSZ; Figure 3C).

The magnetic and bathymetric lineaments closely resemble each other and support the presence of a network with a limited number of continuous ductile E–W to NW–SE zones, and a larger number of shorter zones with an overall cross-cutting feature (Figure 3B-C). The eastern contact of the Åland batholith is pronounced in both datasets, and most of the other rapakivi occurrences also spatially

coincide near the recognized structures: The SkSZ and MSZ bound the occurrence of the Vehmaa batholith, whereas a zone of pronouncedly dense N–S zones cluster immediately east of the Mynälahti SZ (MSZ), deflect east against the Laitila batholith and the Kolinummi SZ, and finally coalesce with the KySZ. A distinct "shadow" with no N–S structures is present north of the Vehmaa batholith. The smaller Fjällskär rapakivi intrusion occurs along the southward continuation of the MSZ, while the Kökar intrusion is spatially associated with a discontinuous corridor of approximately N–S lineaments.

4.2 Types of Brittle Structures

Within the Åland rapakivi intrusion, fault zones and slickenside surfaces (Figure 4A) are rarely available in the field, but small faults composed of shear fractures (Figure 4B) and kinematically related tension fractures are commonly observed. Such fault structures are often composed of multiple shear fractures interlinked by tensional step-over fractures (Figure 4B). Many faults also exhibit en échelon fractures along the path of the fault plane (Figure 4A) or horse tail fractures or wing cracks at the termination of the structures (Figure 4D). Faults in their initial stage in the form of en échelon faults can also be observed (Figure 4E), where deformation terminated before the development of a throughgoing slip surface (fault plane). Although difficult to observe from the eroded bedrock outcrops, occasional thin fillings of quartz were observed in some of the faults and/or reddish alteration halos around some of the fault planes (Figure 4F). In certain locations, the orthomosaic images and digitized fracture traces were also useful for identifying somewhat larger and more distributed fault structures where, for example, step-over structures between more widely separated shear fractures were determined during field mapping (Figure 4G). The individual shear fractures on Geta vary in length between 1.6–221 m, faults between 5–221 m, and fault zones between 40–350 m. It is emphasized, however, that fault zones (Figure 4H) are only rarely observed in the outcrops and the total lengths of these are in many cases impossible to estimate, as they typically extend beyond the outcrops. Hence, the provided length values for most fault zones and many shear fractures are censored and should be considered as minimum bounds.

Joints typically occupy the volumes between fault structures, where they form distinct fracture sets with regards to their orientation (Figure 4I). The joints we mapped on Geta have lengths varying between 8 cm and 150 m, but are only rarely longer than 50 m. Clastic dykes, a couple of centimeters in width, were observed at two locations.

4.3 Relative Age Relationships

Cross-cutting relationships between faults were rarely visible. However, one cross-cutting relation in Geta subregion 5 demonstrates an E-W trending fault predating a ENE-WSW trending one (Figure 5A).

Based on observed cross-cutting relationships from digitized UAV fracture traces (Figure 5B-C) and field observations, joints tend to abut fault structures, thus indicating that the jointing postdates faulting (*Peacock et al.*, 2018; *Skyttä et al.*, 2021). We note that the genetic relationship of individual fractures can sometimes remain uncertain, and some of the larger fractures we have classified as joints could represent secondary fracturing related to adjacent fault structures occurring, for example, beneath neighboring offshore areas.

Mutual abutment and cross-cutting relationships are observed for different subvertical joint sets, which indicates a synchronous age of formation. The two-dimensional character of outcrops makes cross-cutting relationships to horizontal joints difficult to observe. Instead of the orientation, cross-cutting relationships among joints are observed to be more dependent on the length of the individual joints, with shorter joints usually abutting against longer ones (Figure 5D). Consequently, topological relationships between joints are dominated by Y or T intersections, which illustrates that the propagation of joints was limited by interactions between fracture planes.

4.4 Orientation and Paleostress Analysis of Subregions

The five subregions of the Geta outcrop area (Figure 2A) were separately analyzed for orientation, kinematics, and the paleostress states of different fracture and fault datasets. Due to the similarity of lithology and the style of deformation, the size of the subregions was defined based on the availability of fault kinematic observations (paleostress analysis requires at least four fault kinematic observations within each sub-set).

As an example of one individual subregion dataset, including UAV orthomosaics, fracture traces, field classifications, and data, Geta subregion 5 with associated data is presented in Figure 6. Corresponding figures from all Geta subregions are compiled in Supporting Information (Appendix B). Structural analysis results for each subregion are presented in sections 4.4.1 and 4.4.2. For paleostress analysis, we also include fault data from other control sites of the Åland archipelago (Figure 3A).

4.4.1 Kinematics and Paleostress Analysis of Fault Structures

Fault structures at the Geta outcrops are mainly vertical strike-slip faults, with most faults being approximately E–W trending. In addition, a smaller

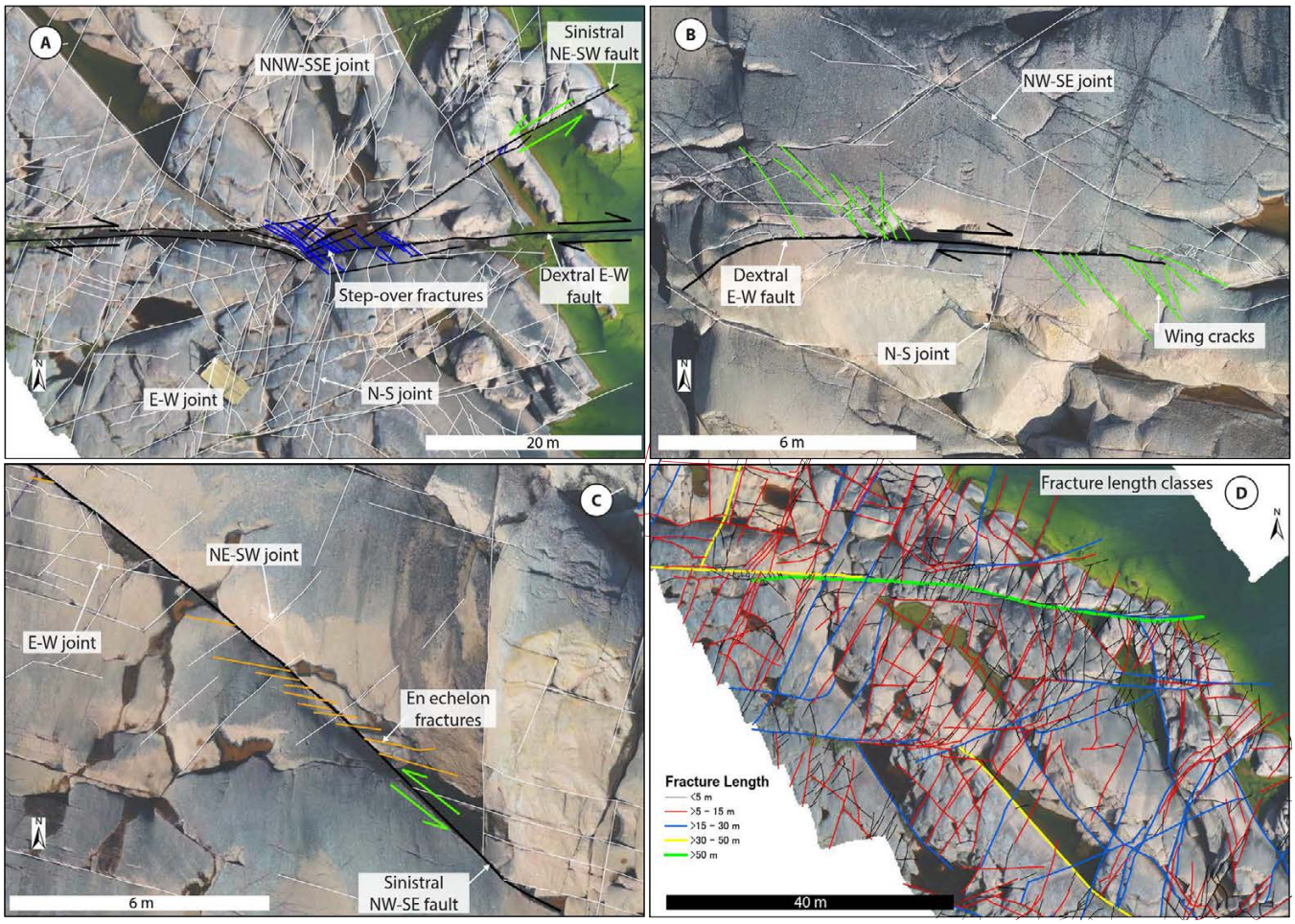

Figure 5 – UAV fracture maps visualizing the relative age relationships between joints and fault structures. **A)** Sinistral NE–SW-trending fault abut an E–W-trending dextral step-over fault. Joints can also be observed abutting both fault structures. **B)** A small-scale E–W-trending dextral fault with wing cracks. Joints abut the fault. **C)** A NW–SE-trending fault with sinistral en échelon fractures along the shear plane. Joints can be observed abutting the fault. **D)** Fracture traces from subregion 5, visualized according to length classes. Kinematics of fault structures in a–c are visualized as double arrows (green arrows for sinistral and black for dextral).

number of N–S-trending subvertical faults also exist (Figure 7A). The E–W-trending faults include both dextral and sinistral ones, while the N–S-trending faults are almost exclusively dextral. The UAV maps in Figure 7A display the location of the 139 faults observed from Geta, separated into sinistral and dextral faults. The stereogram in Figure 7A further displays the orientation of the 118 kinematic fault structure observations that were accepted for paleostress analysis from Geta. Mapped fault structures in Eckerö and Föglö display similar orientations and kinematics to the faults from Geta, while mapped faults on Vårdö are predominantly sinistral and NW-SE-trending, and the fault data from Boxö mainly includes E–W-trending dextral faults (Figure 7B).

The fault-slip data collected from the Geta outcrops were sorted into tectonically compatible sub-sets, which resulted in two sub-sets (Figure 8A) labeled as Stage 1 and Stage 2 faults. Most kinematic observations represent individual shear planes and associated tension fractures. The kinematic observations associated with Stage 1, however, also include a few fault zones and slickensides, while kinematic Stage 2 observations are entirely composed of measurements from individual shear planes with associated tension fractures. Paleostress inversion of the Stage 1 sub-set (Figure 8B), which mainly includes E–W to SW–NE-trending dextral and a few NW–SE-trending sinistral faults and fault zones, results in a strike-slip stress regime with a roughly NW–SE-trending σ_1 stress axis. Corresponding analysis of Stage 2 (Figure 8C), consisting of both E–W-trending sinistral and N–S-trending dextral faults, results in a strike-slip stress regime with a NE–SW-trending σ_1 stress axis. The remaining observations that were omitted from both these sub-sets were assigned to "scatter", as these could not be further processed into other mechanically reasonable sub-sets and paleostress states (Figure 8D). Due to the generally low number of slickenside observations, and low number of fault observations within some of the sub-sets, the quality of calculated stress tensors is typically of intermediate (C) class, however, lower quality (D–E) results were also attained for some of the sub-sets (Table 1).

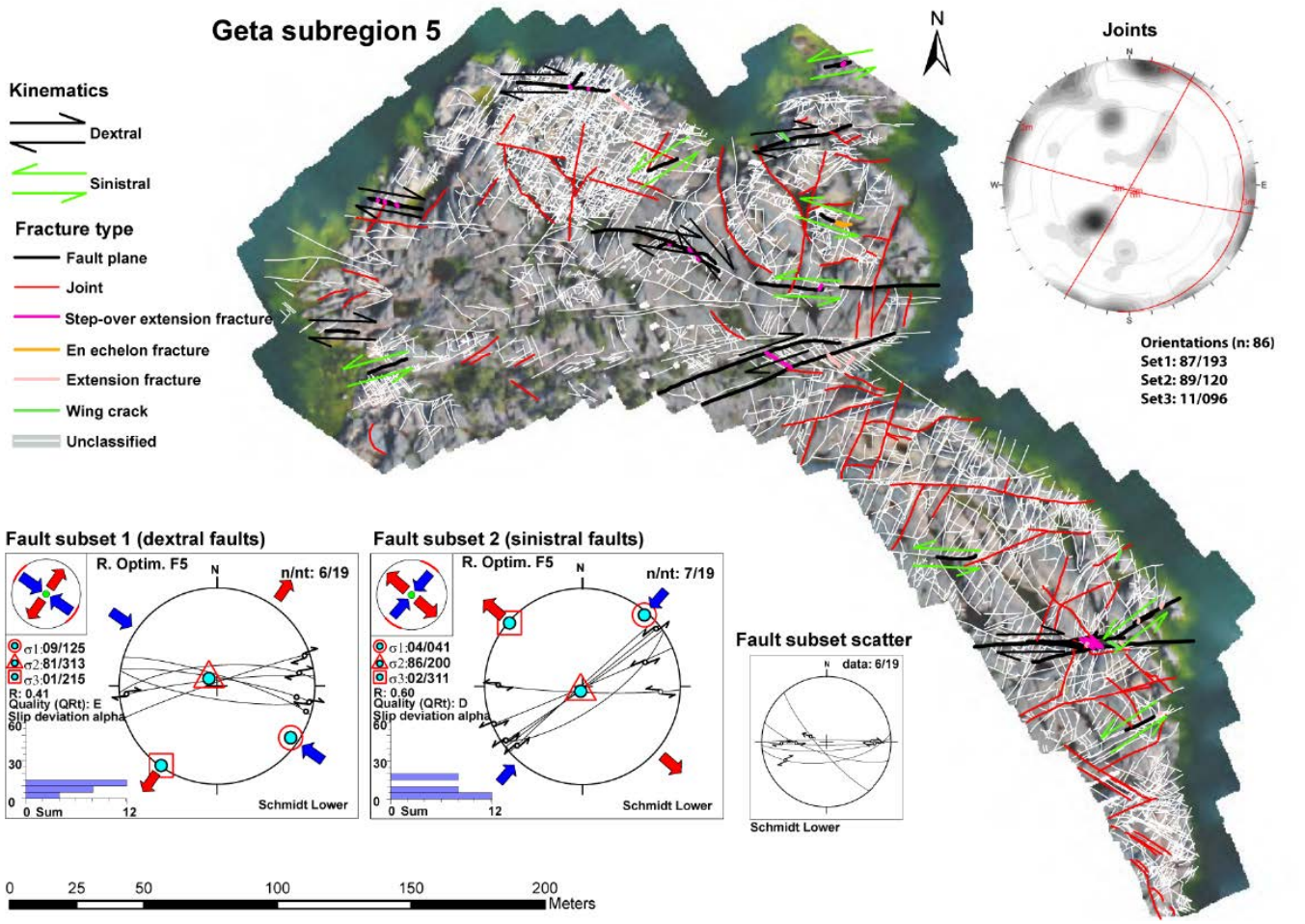

Figure 6 – Example of the fracture and fault dataset from Geta subregion 5. The digitized UAV fracture traces are colored according to type. Lower hemisphere stereonet projections at bottom left show fault data and paleostress inversion results of separated subsets. Stereonet at top right shows orientation of poles to measured joints as contour plot. The orientation maxima of defined fracture sets are given below the stereogram.

To investigate the impact of scale on the kinematics of fault structures, we also divided the Geta fault dataset into length classes of <25 m, 25–60 m, and >60 m (Figure 8E-F). This analysis resulted in similar sub-sets and stress tensors as for all data (Figure 8A-B), which indicates that within the Geta outcrop area, the kinematics of fault structures are independent of scale.

To analyze the spatial variation of the kinematics of faults along the Geta outcrop area, data from the five different subregions were separately analyzed (Figure 9A). Furthermore, to investigate the representativity of the fault data from the Geta outcrop area for the whole Åland rapakivi, and to identify potential broader spatial variations, we also analyzed fault datasets from the control site of Boxö, Vårdö, Föglö and Eckerö outcrop areas (Figure 9B). The sorting and analysis of the Geta subregions (Figure 9A) resulted in similar sub-sets as for all data from Geta (Figure 8), with the Stage 1 faults being compatible with a pure strike-slip stress regime (R = 0.25–0.75) with a WNW–ESE to NW–SE-trending σ_1 stress axis. The Stage 2 sub-set, however, displayed some more variation and slightly different results compared to the total Geta dataset (Figure 8B). Analysis of Stage 2 for the subregions 1 and 2 resulted in transtensive stress regimes (R > 0.75) and subregion 3 in a transpressive (R = < 0.25) one (Figure 9A), which differs from the pure strike-slip regime inferred for the whole Geta area. In addition, a deviating ENE–SES-trending σ_1 stress axis was derived for subregion 3, compared to the NE–SW orientation of the other subregions (Figure 9A) and the total dataset (Figure 8C). Due to the limited amount of data, no Stage 2 sub-set could be calculated for subregion 4.

Analysis of Stage 1 for the Boxö, Vårdö, Föglö and Eckerö datasets yielded corresponding results to the Geta area (Figure 9B), except for the Vårdö dataset, which resulted in a transpressive stress regime. Contrary to the other areas, the Vårdö Stage 1 sub-set mainly includes ESE–WNW-trending sinistral faults (Figure 7B). The Stage 2 results for Boxö, Föglö, and Eckerö are also quite similar to the results from Geta, with pure strike-slip and transtensive stress regimes having comparable σ_1 orientations. Due to a lack of data, no Stage 2 sub-set could be separated for the Vårdö area. Detailed parameters of all calculated paleostress tensors are presented in Table 1.

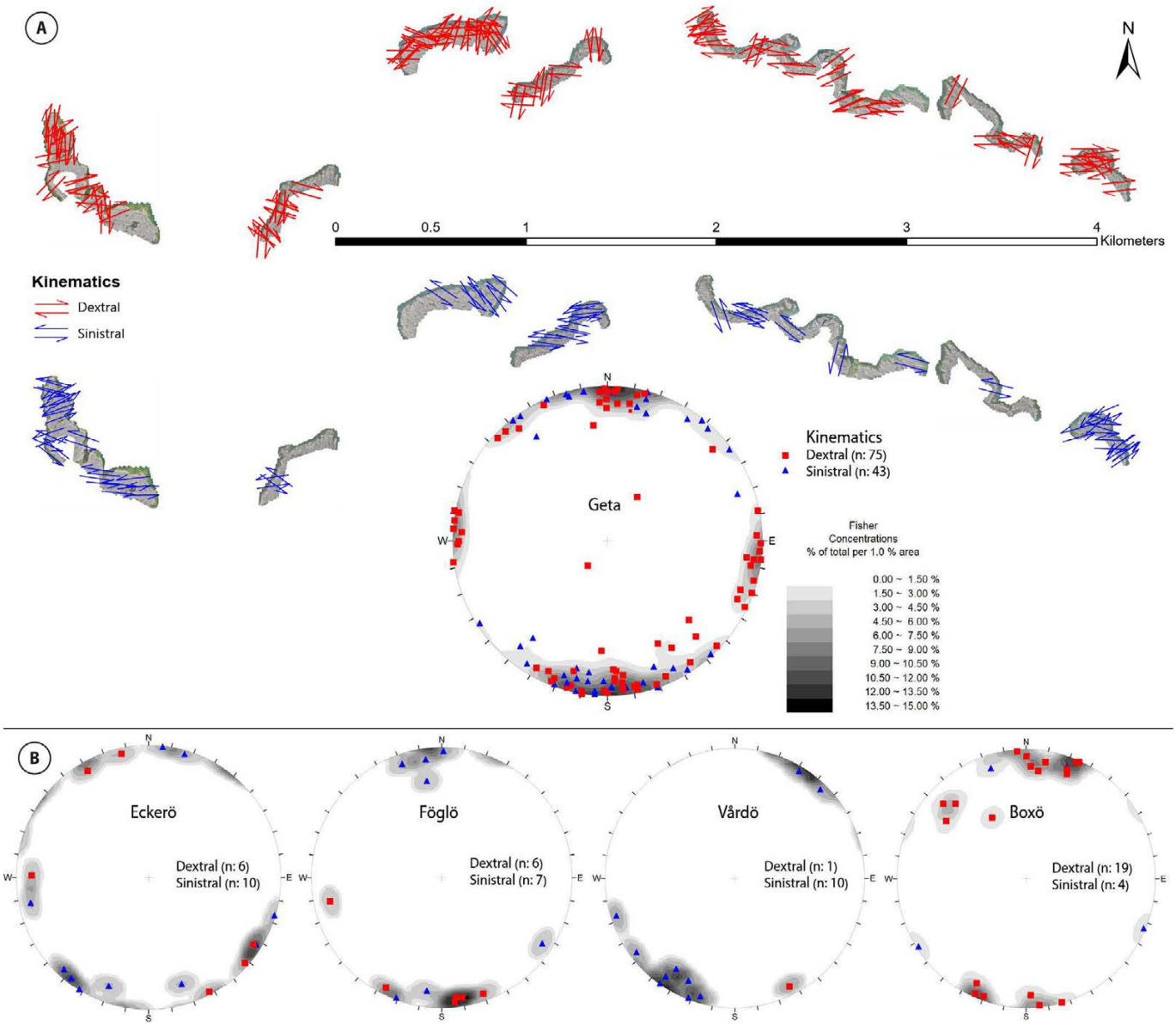

Figure 7 – A) Mapped fault structures (n: 139) from the Geta outcrop area. The location of dextral and sinistral observations is plotted separately on the UAV maps. The stereogram displays the orientation data of the 118 fault observations from Geta that were accepted for paleostress analysis. Red poles = dextral, blue poles = sinistral. **B)** Corresponding stereograms from Eckerö, Föglö, Vårdö, and Boxö areas Figure 3)

4.4.2 Orientation and Paleostress of Joints

Joints in Geta represent mode I fractures (Figure 4I) and consist of three major joint sets that form an orthogonal fracture pattern. Set A consists of E–W to ESE–WNW-trending subvertical joints, Set B of N–S to NE–SW-trending subvertical joints, and Set C of subhorizontal to moderately NE-dipping joints (Figure 10A). The orientation of the main sets is quite consistent along the different subregions of the Geta outcrop area (Figure 10B), although some variation and rotation of individual joint sets between subregions and within individual bedrock blocks of individual subregions is observed. This indicates that the stress state during joint formation was relatively constant throughout the area and there is no further need to divide the data into smaller subsets with respect to paleostress analysis.

The subhorizontal Set C is not very prominent in the subregion 1 dataset (Figure 10C), partly due to the horizontal and two-dimensional nature of the outcrops of subregion 1 (and certain parts of the other subregions), which limits the possibilities to map horizontal to subhorizontal fractures.

Based on the GArcmB mixed Bingham distribution analysis (Figure 10D), all three sets have small stress ratios (R) of 0.2–0.3 (a small difference between the magnitudes of σ_2 and σ_3). The resulting σ_1 orientation is vertical for Set A and B joints and horizontal for Set C. Set A joints were formed in pure extension, Set B in radial extension, and Set C in pure compression. The main parameters of the different fracture sets, including the orientation, stress axes, concentration parameters, stress ratio, and modified stress regime index, are given in Table 2.

Table 1 – Paleostress tensors derived from the processed fault-slip data.

Source	n	Total	% Total	σ_1 Plunge	σ_1 Trend	σ_2 Plung	σ_2 Trend	σ_3 Plunge	σ_3 Trend	R	R'	Regime	Tensor Type	Quality	Stage
Geta area	50	121	41.3	01	121	88	247	01	031	0.4	1.6	Strike-Slip	Pure strike-slip	C	1
Geta <25 m	12	43	27.9	09	292	79	148	06	023	0.39	1.61	Strike-slip	Pure strike-slip	C	1
Geta 25-60 m	13	42	31.0	04	124	85	265	03	034	0.5	1.5	Strike-slip	Pure strike-slip	E	1
Geta >60 m	11	36	30.6	02	292	85	179	05	022	0.34	1.66	Strike-slip	Pure strike-slip	C	1
Geta 1	7	37	18.9	24	098	62	312	14	194	0.59	1.41	Strike-slip	Pure strike-slip	E	1
Geta 2	13	36	36.1	02	102	88	282	00	192	0.26	1.74	Strike-slip	Pure strike-slip	C	1
Geta 3	7	16	43.8	08	287	77	159	10	018	0.37	1.63	Strike-slip	Pure strike-slip	D	1
Geta 4	6	13	46.2	03	132	87	295	01	042	0.52	1.48	Strike-slip	Pure strike-slip	D	1
Geta 5	6	19	31.6	09	125	81	313	01	215	0.41	1.59	Strike-slip	Pure strike-slip	E	1
Eckerö	6	16	37.5	05	312	84	098	02	222	0.52	1.48	Strike-slip	Pure strike-slip	D	1
Föglö	6	13	46.2	09	125	81	322	03	215	0.52	1.48	Strike-slip	Pure strike-slip	D	1
Vårdö	7	11	63.6	10	286	68	041	20	193	0.1	1.9	Strike-slip	Trans-pression	D	1
Boxö	14	23	60.9	02	301	75	038	15	210	0.26	1.74	Strike-slip	Pure strike-slip	C	1
Geta area	48	121	39.7	00	053	86	317	04	143	0.44	1.56	Strike-slip	Pure strike-slip	C	2
Geta <25 m	15	43	34.9	04	220	83	096	06	310	0.16	1.84	Strike-slip	Trans-pression	C	2
Geta 25-60 m	18	42	42.9	02	067	86	306	03	157	0.83	1.17	Strike-slip	Trans-tension	C	2
Geta >60 m	16	36	44.4	04	231	84	000	05	141	0.75	1.25	Strike-slip	Trans-tension	C	2
Geta 1	22	37	59.5	13	045	77	224	00	315	0.97	1.03	Strike-slip	Trans-tension	C	2
Geta 2	14	36	38.9	07	053	79	283	08	144	0.76	1.24	Strike-slip	Trans-tension	C	2
Geta 3	6	16	37.5	02	258	85	012	05	168	0.23	1.77	Strike-slip	Trans-pression	D	2
Geta 5	7	19	36.8	04	041	86	200	02	311	0.6	1.4	Strike-slip	Pure strike-slip	D	2
Eckerö	9	16	56.3	14	240	73	022	10	147	0.7	1.3	Strike-slip	Pure strike-slip	D	2
Föglö	7	13	53.8	11	241	77	094	07	332	0.79	1.21	Strike-slip	Trans-tension	D	2
Boxö	4	23	17.4	06	249	80	123	08	340	0.47	1.53	Strike-slip	Pure strike-slip	E	2

Table 2 – Joint set orientation and paleostress results.

Joint set	Mean Orientation		Principal Stress Axes			Concentration		Stress Ratio	R'
	DIP	DIR	σ_1	σ_2	σ_3	K_1	K_2		
Set A	88	188	264.6/79.3	095.1/10.5	004.7/01.9	-21.049	-6.309	0.2997	0.2997
Set B	89	285	199.3/83.9	015.2/06.1	105.2/00.4	-19.980	-3.969	0.1986	0.1986
Set C	12	031	114.9/00.6	024.7/16.4	206.9/73.6	-7.918	-2.534	0.3201	2.3201

5 Discussion

5.1 Paleostress Stages and Relative Age Relationships of Brittle Structures on Åland

It has been questioned if fault-slip inversion analysis can reveal actual paleostresses and, if so, to which degree such results can be used to describe regional stresses rather than more local strain directions (e.g., *Lacombe*, 2012; *Riller et al.*, 2017). For example, the justification of the subdivision of heterogeneous and sparse fault slip-datasets into homogeneous subsets has been questioned (*Riller et al.*, 2017). Acknowledging the above, we regard the fault datasets from the Åland rapakivi particularly

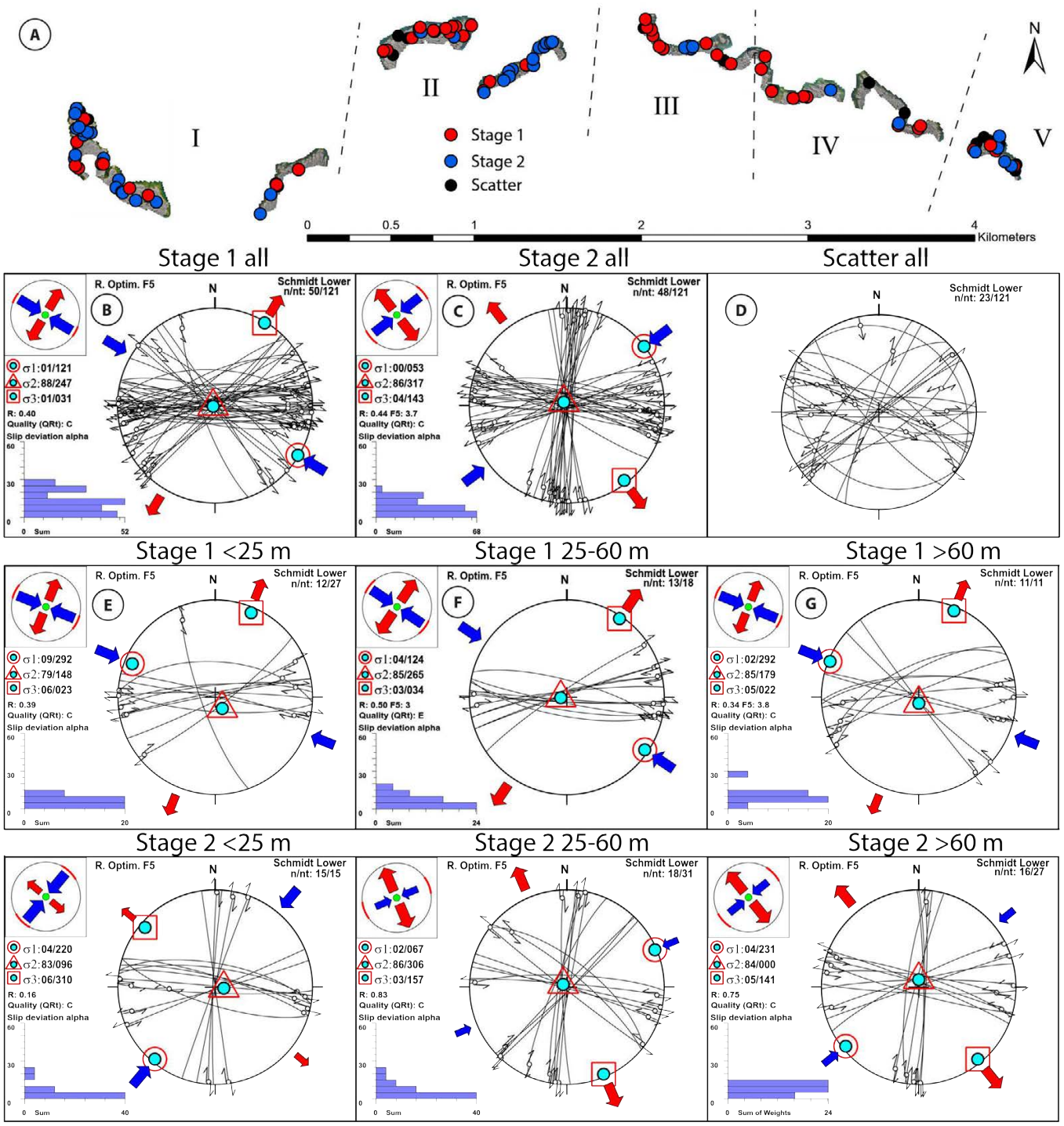

Figure 8 – Summary of the WinTensor paleostress inversion analysis results for the Geta outcrop area. **A)** Location of kinematic fault observations visualized on the UAV map according to Stage 1 (red), Stage 2 (blue) and "scatter" (black) sub-sets. **B)** Stage 1 strike-slip regime with NW–SW compression based on all fault observations. **C)** Stage 2 strike-slip regime with NE–SW compression based on all fault observations. **D)** Scatter that was omitted from both Stage 1 and 2. **E)** Strike-slip regime with ENE–WSW compression (Stage 1) and transpressional regime with NE–SW compression (Stage 2) based on faults <25 m in length. **F)** Strike-slip regime with NW–SE compression (Stage 1) and transtensional regime with ENE–WSW compression (Stage 2) based on faults 25–60 m in length. **G)** Strike-slip regime with WNW–ESE compression (Stage 1) and transtensional regime with NE–SW compression (Stage 2) based on faults >60 m in length.

well suited for such analysis due to the following: a) the anorogenic and isotropic rapakivi batholith lacks ductile precursors that could have affected fault localisation within the outcrop scales, b) our results are consistent throughout the batholith and c) density of observations for the Geta outcrops (Figure 9) are high enough to reveal potential local anisotropies. Consequently, we argue that the rapakivi behaved as relatively isotropic medium during brittle deformation and that our results adequately represent the regional paleostress fields that were relatively uniform for the Åland rapakivi batholith, at least for the first generation of faults within the outcrop scales.

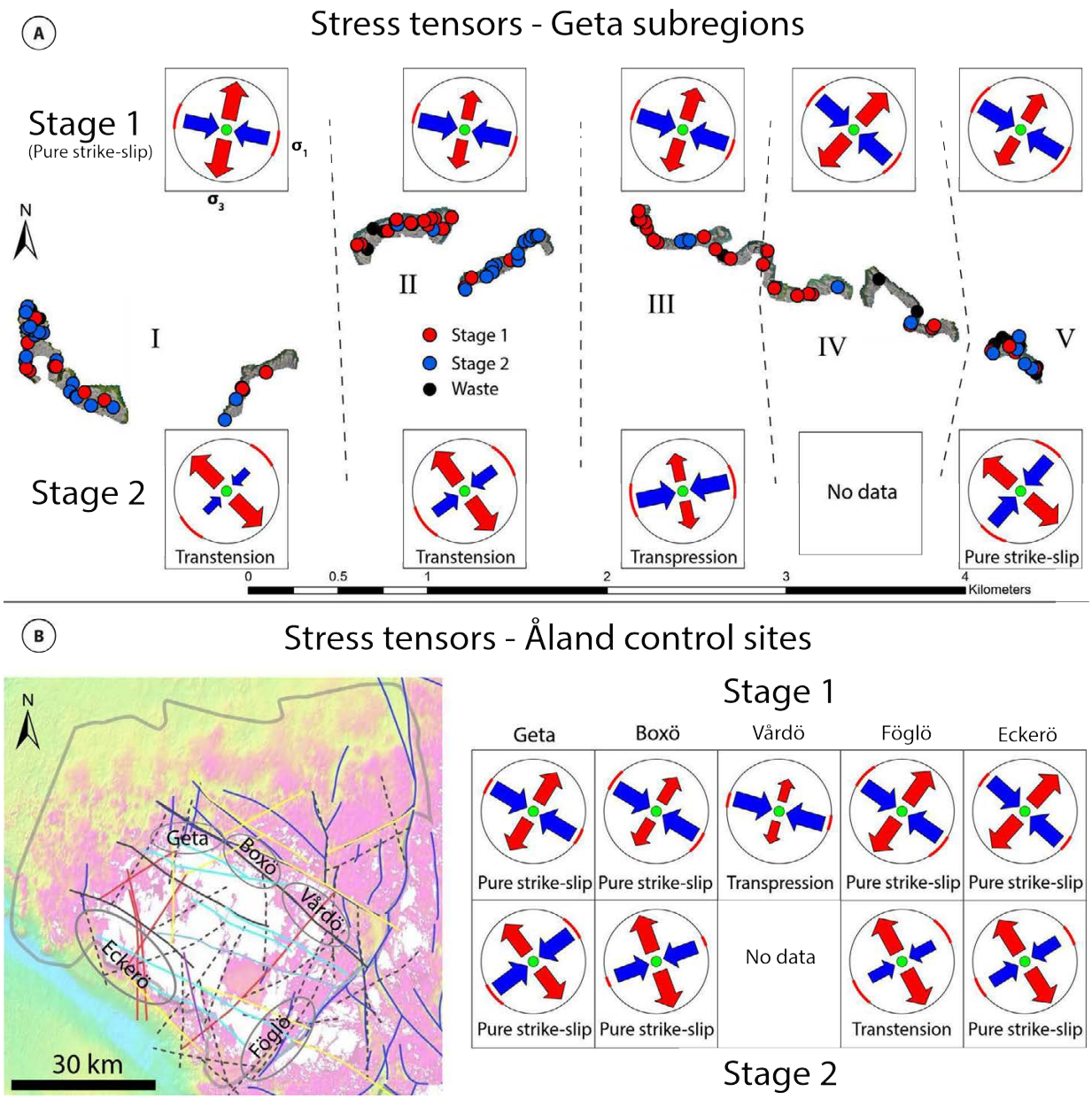

Figure 9 – **A)** Overview of the determined stress regimes for subregions of the Geta outcrop area. **B)** Overview of the determined stress regimes for Geta, Boxö, Vårdö, Föglö and Eckerö outcrop areas. The location of outcrop areas is visualized on top of the Figure 3A lineament map. The σ_1 stress axis is displayed in stress symbols by the blue converging arrows and σ_3 by the red diverging ones. A pure strike-slip stress regime is represented by arrows of similar size, a transpressive stress regime by smaller red diverging arrows and a transtensive stress regime by smaller blue converging arrows.

Paleostress analysis of fault kinematic datasets from within the Åland rapakivi resulted in two different sub-sets, representing two different stages of strike-slip faulting, which we have termed Stage 1 and Stage 2 (Figure 8 and Figure 9). The Stage 1 and Stage 2 stress tensors for the Geta outcrop area are compatible with strike-slip stress regimes characterized by WNW–ESE to NW–SE and NE–SW main compressive stress axis (σ_1) trends, respectively (Figure 8). The paleostress results for Stage 1, both for the relatively small sub-areas within the higher-resolution Geta outcrop area and the regional control sites (Figure 9), are uniform. Consequently, the paleostress field during Stage 1 may be considered uniform across the whole study area, and the studied volumes appear to represent a coherent tectonic unit (*Sperner and Zweigel*, 2010). By contrast, Stage 2 results display slightly larger variation of the orientation of principal stress tensors between both the sub-areas of the Geta outcrop area and the regional control sites (Figure 9A-B). Variation is also evident from the presence of local transtensive stress regimes within the strike-slip-dominated Stage 2.

We attribute the higher spatial variability of paleostress orientations during Stage 2 to the presence of pre-existing structures, and the resulting higher level of mechanical anisotropy in the bedrock during Stage 2, which caused the perturbation of the stress field and higher heterogeneity of the resulting brittle structures (*Pollard*, 1987; *Maerten*

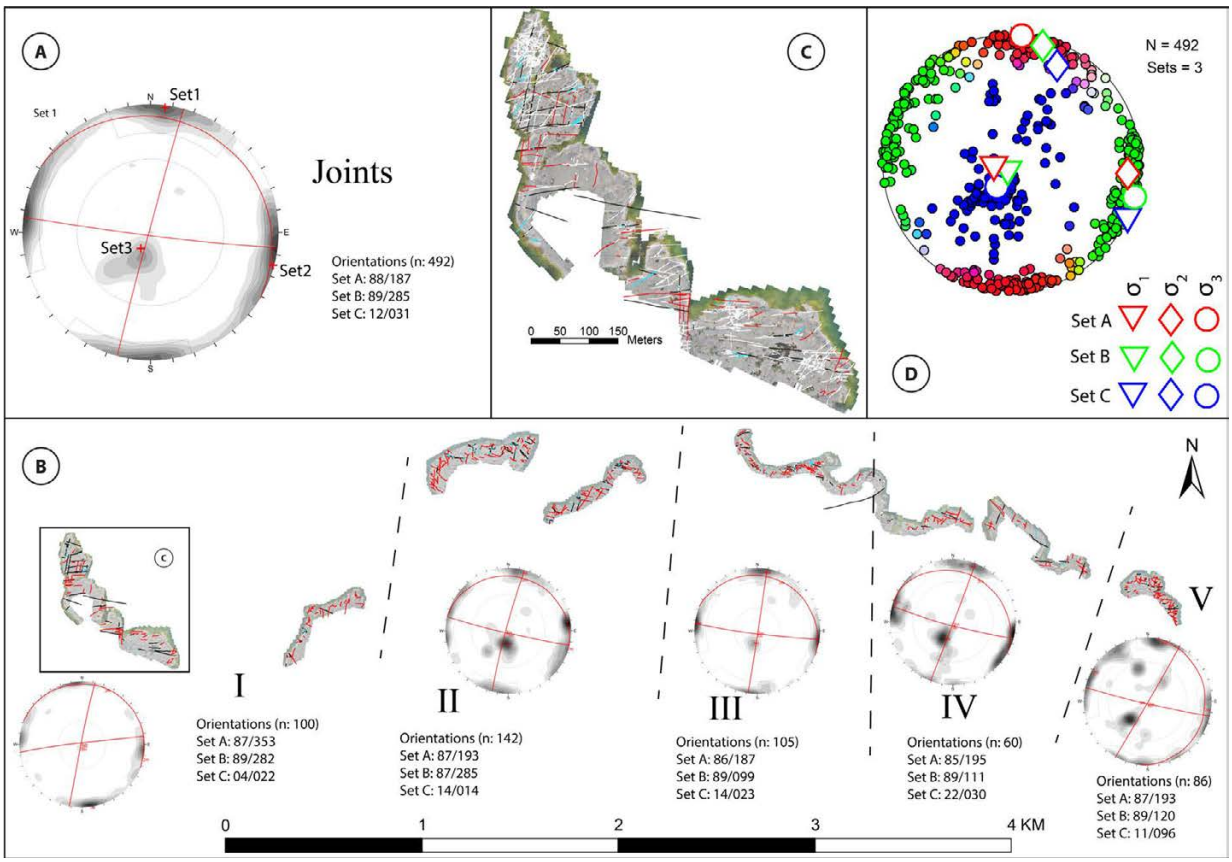

Figure 10 – Distribution of joint orientations across the Geta outcrop area. **A)** Joint orientation distribution of the whole Geta outcrop area. **B)** The orientation distributions separately for all subregions. Joint traces on the maps are presented in red, fault planes in black, and other fracture classes in blue. Unclassified traces are not visualized. **C)** Zoom-in to an outcrop in subregion 1, including visualization of unclassified fracture traces in white. **D)** Mixed Bingham distributions for the three sets, generated with GArcmB software. All stereograms are equal area and lower hemisphere projections.

et al., 2002; *Skyttä et al.*, 2021). This is in line with the presented relative timing between faulting Stages 1 and 2, and with the formation of Stage 1 structures into undeformed and mechanically isotropic bedrock. The few available cross-cutting relationships between the mapped faults support the relative timing of faulting stages resulting from the paleostress analyses: an ENE–WSW-trending sinistral fault probably associated with Stage 2 abuts a distinct E-W-trending dextral fault of Stage 1 (Figure 5C).

The observed joints terminate systematically against all faults within the study area (Figure 5), which shows that both faulting stages pre-dated the formation of most joints (Peacock et al., 2018). Based on the mixed Bingham distribution analysis of joints (Figure 10), both Set A (E–W-trending vertical) and Set B (N–S-trending vertical) joints were formed in an extensional stress regime characterized by an approximately vertical σ_1 stress axis, while the orientation of the subhorizontal σ_2 for Sets A and B had E–W and N–S trends, respectively. The mutual abutment and cross-cutting relationships (Figure 5) between Set A and Set B joints indicates a synchronous age of formation for these two fracture sets (*Peacock et al.*, 2018). Moreover, the similar orientation of σ_1 and the small stress ratio for both sets further justifies the synchronous timing of joint Sets A and B, as only small local variations in the stress field are required to generate the orthogonal joint pattern (*Bai et al.*, 2002). For horizontal Set C joints to develop, a lower relative magnitude of normal stress (vertical σ_3) is required, which thereby requires a greater modification of the regional stress field from that during Stages 1 and 2 (from a vertical σ_1 to a vertical σ_3).

Regional joints may have diverse origins, which are difficult to trace (*Pollard and Aydin*, 1988), but the formation of joints is generally attributed to burial and/or exhumation processes of the bedrock (*English*, 2012). *Nadan and Engelder* (2009) demonstrated that thermoelastic relaxation and isobaric cooling during the exhumation of intracontinental granitoids causes development of early vertical microcracks, interchanges between σ_2 and σ_3, and late horizontal cracks. Due to the exhumation of the rapakivi from a 5–10 km depth to the surface between Mesoproterozoic and Cambrian times, we suggest that the vertical joints of Sets A and Set B within the Åland rapakivi developed in response to similar thermoelastic relaxation (*Nadan and Engelder*, 2009) during post-faulting exhumation processes of the bedrock (Figure 11). Furthermore, we also suggest that the formation of horizontal Set C jointing occurred after Set A and Set B, and possibly at a higher crustal level with lower normal stress. The cross-cutting relationships with Set C were not

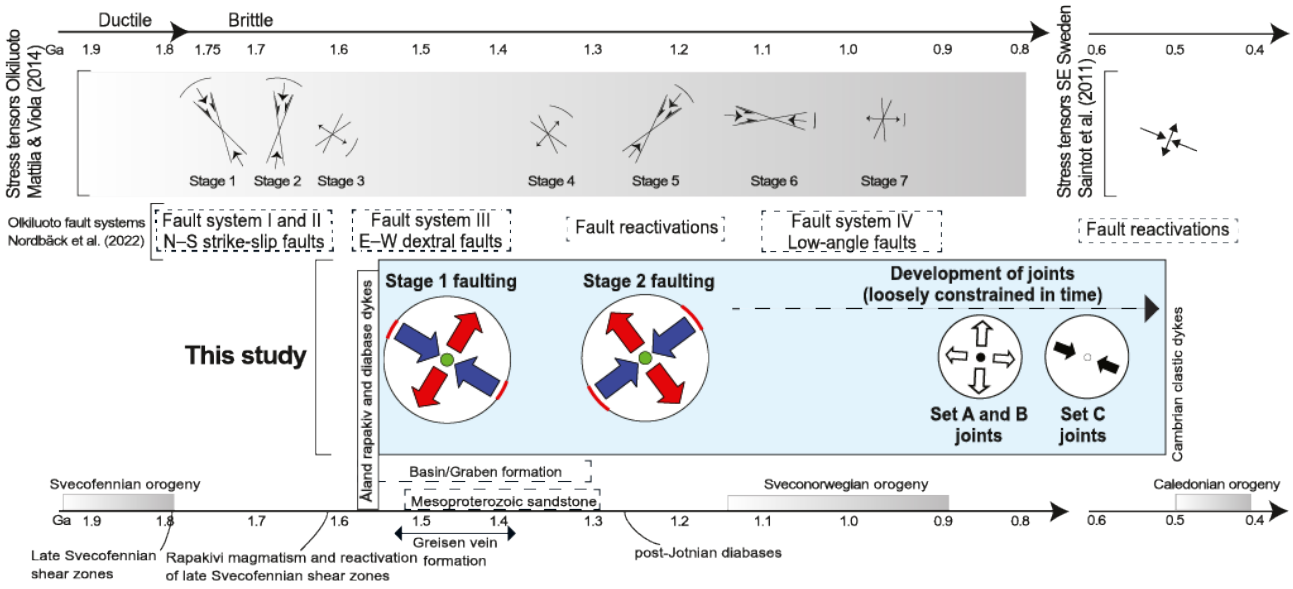

Figure 11 – Chronological model for the timing of the two faulting stages and later formed joints within the Åland rapakivi. The sequence of these events is based on relative age relationships and the structural interpretations of this study. The timing of events is estimated based on correlations with previously published results, and thus only loosely constrained in time. The results of this study are compared with the paleostress results of *Mattila and Viola* (2014) and *Saintot et al.* (2011), isotopic and structural results of *Nordbäck et al.* (2022), and with other major tectonic events of the Fennoscandian shield. Figure modified after *Mattila and Viola* (2014).

possible to investigate as part of this study due to the two-dimensional nature of the outcrops, and consequently the scarce amount of these joints in our datasets.

Additional evidence of the relative age relationship between faulting stages and jointing is provided by the two subvertical joint sets that at the Boxö control site trend parallel and perpendicular to the major NW–SE-trending Boxö lineament (*Kraatz*, 2022). Thus, the joint set orientations in Boxö deviate from those in the Geta outcrop area, which could indicate local stress disturbances caused by the vicinity of a large fault zone. Moreover, a slight progressive clockwise rotation of the joint orientation sets between the subareas of the Geta outcrop from west to east (Figure 10) could be attributed to the decreasing distance from the Boxö fault, indicating that the fault contributed to stress heterogeneity during the formation of the regional joints.

5.2 Correlation with Brittle Structural Evolution within Fennoscandia

The maximum age of faults recognized in this study (Stages 1 and 2) is constrained by the crystallization age of the hosting 1.58 Ga Åland batholith (*Suominen*, 1991), whereas no suitable absolute age determinations are available to constrain their minimum age. However, similarly as previously observed within the 1.65–1.62 Wiborg rapakivi (*Skyttä et al.*, 2021), regional joints of the Åland rapakivi abut the pre-dating faults (Section 4.3). The minimum age of jointing can be inferred to be ca. 540 Ma from the occurrence of Cambrian clastic veins (*Bergman et al.*, 1982), which, based on their common orientation with the Set B joints, are Set B joints that have been filled with sediments. Since joints can develop at variable depths within the crust (*Gillespie et al.*, 2001), the subvertical joints (Set A and B) most likely already developed prior to being exhumed at the Cambrian erosional surface. Hence, we infer that the faulting stages 1 and 2 of this paper occurred at some time between 1.58 and 0.54 Ga (Figure 11).

The paleostress conditions determined for the faulting stages of this investigation are not unequivocally compatible with the suggested overall extensional regime associated with rifting between 1.6–1.3 Ga (*Korja et al.*, 1993; *Saintot et al.*, 2011; *Mattila and Viola*, 2014; *Tillberg et al.*, 2020, 2021) or the earlier available paleostress constraints covering the brittle crustal evolution of Fennoscandia (*Heeremans and Wijbrans*, 1999; *Saintot et al.*, 2011; *Mattila and Viola*, 2014; *Tillberg et al.*, 2020, 2021; *Nordbäck et al.*, 2022). However, several pieces of evidence indicate that the faults observed in this study were initiated during a time interval between 1.6 and 1.2 Ga: Faulting or veining following the rapakivi magmatism has been observed in the form of (i) the formation of sinistral N–S-trending faults within the 1.65–1.62 Ga Wiborg rapakivi batholith (Figure 12; *Rämö and Haapala*, 2005; *Skyttä et al.*, 2021), (ii) slip along the Porkkala-Mäntsälä shear zone (*Heeremans and Wijbrans*, 1999; *Kosunen*, 1999), (iii) the formation of E–W-trending dextral faults of Fault system III in Olkiluoto (*Nordbäck et al.*, 2022), (iv) the generation of greisen veins within and around the 1.55 Ga Väkkärä rapakivi granite, Olkiluoto area (*Vaasjoki*, 1996) and (v) the NE–SW extensional stress regime at 1.3–1.4 Ga (*Mattila and Viola*, 2014).

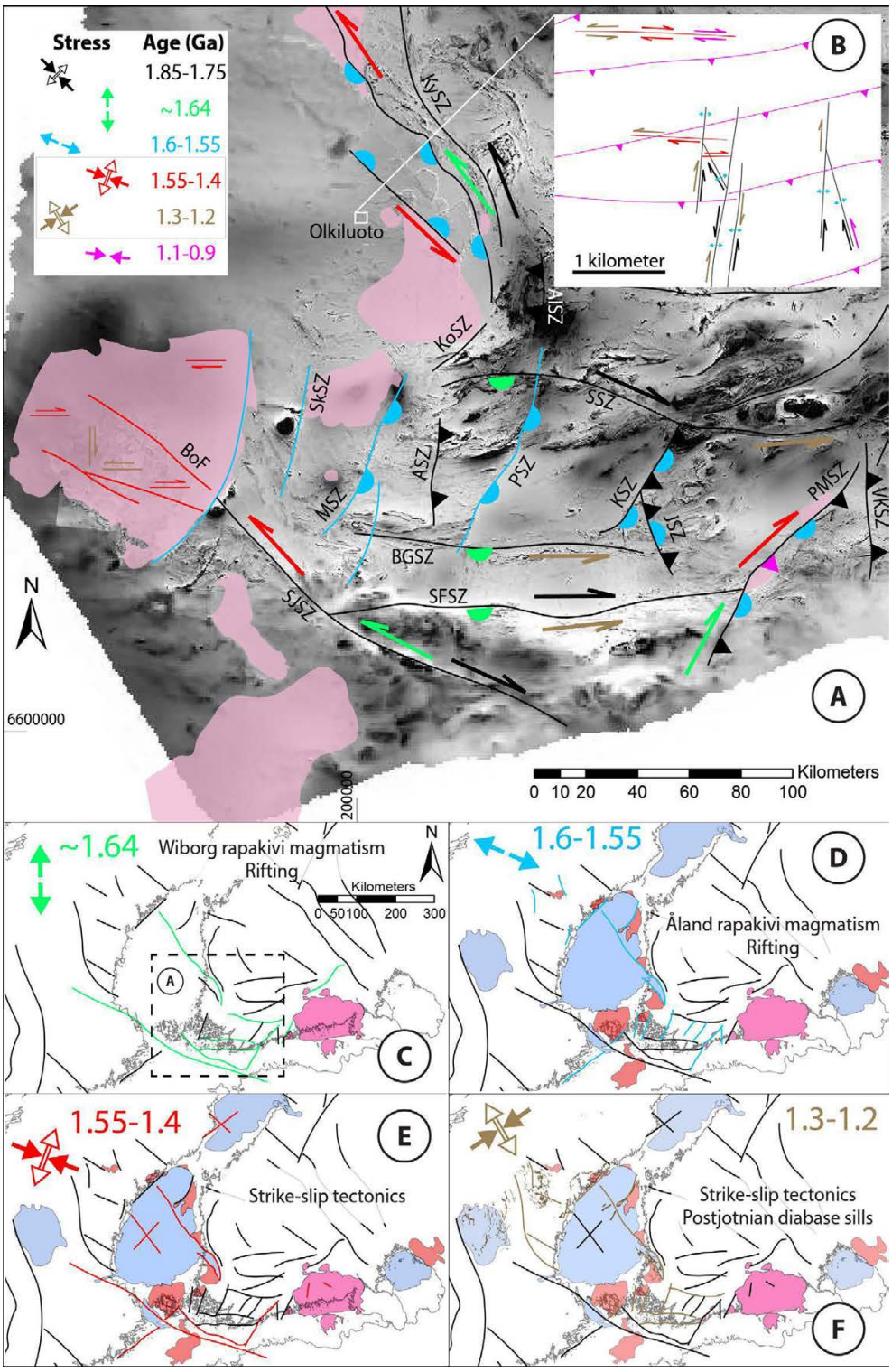

Figure 12 – Model for the Proterozoic structural development of large-scale shear zones and fault zones of southwestern Finland. **A)** Major structures visualized on top of the aeromagnetic map (Geological Survey of Finland, 2007a), with the location of rapakivi granites in light red. The age of the structures and subsequent reactivations are visualized according to color of the tectonic stages in the upper left corner, which are based on previously published results (*Branigan*, 1987; *Nironen*, 1997; *Heeremans and Wijbrans*, 1999; *Väisänen and Skyttä*, 2007; *Torvela et al.*, 2008; *Torvela and Ehlers*, 2010; *Kraatz*, 2013; *Mattila and Viola*, 2014; *Pitkälä*, 2019; *Nordbäck et al.*, 2022) and the results and interpretations of this study (Stage 1 and 2 outlined with gray box). Arrows on the map indicate strike-slip faulting, half-circles normal faulting and triangles thrust faulting. AlSZ = Alastaro Shear Zone, ASZ = Aulanko Shear Zone, BGSZ = Björkö-Gullkrona Shear Zone, BoF = Boxö Fault, MSZ = Mynälahti Shear Zone, PMSZ = Porkkala-Mäntsälä Shear Zone, PSZ = Paimio Shear Zone, SJSZ = Sottunga-Jurmo Shear Zone, SkSZ = Skiftet Shear Zone, JSZ = Jyly Shear Zone, KSZ = Kisko Shear Zone, KoSZ = Kolinummi Shear Zone, KySZ = Kynsikangas Shear Zone, SSZ = Somero Shear Zone, VKSZ = Vuosaari-Korso Shear Zone. **B)** Main fault systems of Olkiluoto (*Nordbäck et al.*, 2022). **C-F)** Geodynamic model for central Fennoscandia during different Mesoproterozoic tectonic stages. The stress field and the proposedly reactivated or newly formed major structures are coloured equivalently. Rapakivi granites are visualized in red, Mesoproterozoic sandstone in blue and Postjotnian diabase in brown.

Available timing constraints for the above include 1.55–1.4 Ga Ar/Ar ages (*Heeremans and Wijbrans*, 1999) from the Obbnäs Rapakivi granite intrusion (Figure 12) in the vicinity of the Porkkala-Mäntsälä shear zone. Furthermore, the circulation of hydrothermal fluids within Fault system III of Olkiluoto (*Aaltonen et al.*, 2018; *Nordbäck et al.*, 2022) indicates that these faults were active during or soon after the emplacement of the rapakivi granites, i.e., at ≤1.6 Ga, and greisen veins have been constrained in age to between 1.56–1.37 Ga (*Mattila and Viola*, 2014). According to the analysis and interpretations of structural data from greisen veins in the Olkiluoto area by *Mattila and Viola* (2014), the regional stress field could have experienced a switch from WSW–ENE extension to NNW–SSE/NW–SE compression during or soon after the formation of the greisen veins. Thus, the compression inferred from the greisen data (*Mattila and Viola*, 2014) is compatible with Stage 1 of this study, the sinistral N–S faults in the Wiborg Batholith (*Skyttä et al.*, 2021) and with the formation of the E–W-striking dextral faults of Fault system III in Olkiluoto (*Nordbäck et al.*, 2022). Based on the above, we tentatively suggest that Stage 1 of this study represents a switch from extension to compression in a strike-slip stress regime that widely affected the crust, at least within the area of present-day southern Finland, soon after the emplacement of the rapakivi batholiths at around 1.55–1.4 Ga (Figure 11).

Faulting Stage 2 of this investigation can be correlated with a K-Ar isotopically dated 1.3–1.2 Ga tectonic event in Olkiluoto (*Nordbäck et al.*, 2022), which is associated with the reactivation of earlier-formed fault systems at the time of intrusion of Postjotnian diabase sills (*Suominen*, 1991), and further with the earlier recognized NE–SW crustal compression (Figure 11; *Mattila and Viola*, 2014). Considering further alternatives for correlations, Stage 1 of this study could also be compatible with the E–W to WNW–ESE compression during the 1.1–0.9 Ga Sveconorwegian orogeny (*Saintot et al.*, 2011; *Mattila and Viola*, 2014). However, this correlation would imply that Stage 1 was younger than Stage 2, which conflicts with our field observations discussed in the previous section. In addition, all Sveconorwegian deformation recognized in Olkiluoto lack any signs of hydrothermal alterations (*Nordbäck et al.*, 2022) such as have been observed in both the N–S trending faults in the Wiborg rapakivi (*Skyttä et al.*, 2021) and the E–W trending faults in the Åland rapakivi (Figure 4F). However, to validate our interpretations and to add more constraints about the timing of faulting, future studies integrating isotopic dating of fault gouge samples are required.

5.3 Relationship between Rapakivi Magmatism, Sedimentary Basins, and Major Structures

We performed a regional structural analysis regarding the relationship between rapakivi magmatism, sedimentary basins and major structures by utilizing bathymetric, topographic, and geophysical data and previously published results. The major structural discontinuities, observed as lineaments, within the Åland rapakivi display NW–SE and NE–SW trends (Figure 3A), which contrasts with the dominantly E–W and N–S-trending fault structures mapped on the Geta outcrops (Figure 7). We suggest that these major lineaments within the rapakivi batholith represent strain localization and the reactivation of pre-existing major shear zones (such as the SJSZ) and fault zones of the Paleoproterozoic bedrock surrounding the Mesoproterozoic rapakivi batholith.

The large scale regional network of structural discontinuities and lineaments (Figure 3B-C) allows us to further link the emplacement of the rapakivi batholiths with reactivation of specific deformation zones. For example, the spatial coincidence of the N–S-trending structures (Figure 3C) and the margins of the <1.6 Ga rapakivi granites of southwestern Finland can be explained by extensional reactivation of the Paleoproterozoic shear zones, which may have acted both as the pathways for the rapakivi magma and created the space for magma emplacement. This interpretation, regarding the structural control on the emplacement of rapakivi granites, is hence in line with the previously proposed E–W to NW–SE extensional tectonics during the intrusion of the Mesoproterozoic rapakivi granites (*Korja et al.*, 2001; *Bingen et al.*, 2008b; *Mattila and Viola*, 2014) and the coeval emplacement of swarms of NE–SW-trending diabase dykes (*Ehlers and Ehlers*, 1977; *Suominen*, 1991). Moreover, nucleation of the NNE–SSW-trending Paimio Shear Zone (PSZ; Figure 12), which displays both brittle characteristics and normal kinematics (*Väisänen and Skyttä*, 2007), highlights that new N–S faults were probably formed during the extensional period preceding the intrusion of the Åland rapakivi batholith.

Furthermore, in the light of the substantial Mesoproterozoic and Paleozoic infill within the Bothnian Basin (Figure 1), reactivation of the N–S structures must have been much more substantial than reactivation of the E–W structures. Thus, within a broader tectonic context, the development of the large-scale structures observed as lineaments and the faulting stages we have observed within the outcrop scales could be related to the development of the Mesoproterozoic sedimentary basin (*Kohonen and Rämö*, 2005) beneath the Bothnian Sea (Figure 1), which can be further linked to the global tectonic processes associated to the rifting prior and during the break-up of the supercontinent Columbia at around 1.3 Ga (*Roberts*, 2013). Compared to previous models describing stable/extensional conditions for the Mesoproterozoic within central Fennoscandia (e.g., *Bingen et al.*, 2008b; *Bogdanova et al.*, 2008), our study finds evidence of a potentially more complex evolution involving a switch from extension to compression between 1.55–1.4 Ga (Stage 1). The

cause for such a change in tectonics is currently unknown, but it is tempting to speculate on a possible link between a change to strike-slip during Stage 1 and the failed rifting beneath the Bothnian basin. As such, our study provides some clues to the largely unknown global evolution during the so-called 1.8–0.8 Ga "Boring Billion" (*Roberts*, 2013), which less boringly includes significant global tectonic events such as the formation and later break-up of the Columbia supercontinent (*Zhao et al.*, 2002; *Hou et al.*, 2008; *Li et al.*, 2008; *Viola et al.*, 2011; *Roberts*, 2013), the formation of large volumes of red-bed sediments and the evolution of eukaryotes (*Parfrey et al.*, 2011; *Rasmussen et al.*, 2020).

By combining the previously published work and the new contributions within this paper, we summarize the current understanding of the Proterozoic tectonic development of major structures within southwestern Finland as follows (see also Figure 12):

1. Late Svecofennian 1.83–1.80 Ga NW–SE to NNW–SSE compression (*Engström et al.*, 2022) caused the formation of ductile to brittle shear zones that steered subsequent brittle deformation (*Torvela and Ehlers*, 2010). For example, the N–S trending strike-slip faults in Olkiluoto (Figure 12B) already formed at the brittle-ductile transition at around 1.75 Ga (*Marchesini et al.*, 2019; *Prando et al.*, 2020).
2. Based on the documented strike-slip reactivation of the SJSZ (*Torvela et al.*, 2008) and the PMSZ (*Elminen et al.*, 2008), N–S regional extension at around 1.64 Ga could have reactivated E–W-trending structures (LSGM; Figure 1), which we attribute to the emplacement of the pre-1.6 Ga rapakivi granites (Figure 1; Figure 12C) of southern Finland along a loosely defined E–W belt (*Nironen*, 1997) (Nironen, 1997).
3. E–W to NW–SE extensional tectonics, preceding or coeval with the intrusion of the 1.58 Ga Åland rapakivi, diabase dykes, and the development of a sedimentary basin beneath the Bothnian Sea caused normal faulting and the reactivation of older N–S trending structures (Figure 12D).
4. WNW–ESE to NNW–SSE compression between 1.55–1.4 Ga (Stage 1 of this study) caused the reactivation of suitably oriented pre-existing structures (Figure 12E) and the development of new small-scale E–W-trending dextral faults within the Åland rapakivi batholith (Figure 12A).
5. NE–SW compression at around 1.3–1.2 Ga, within a strike-slip or transtensional stress regime, caused the reactivation of previously formed brittle structures, the intrusion of diabase sills (Figure 12F) and the development of Stage 2 faults within the Åland rapakivi granite (Figure 12A).
6. NW–SE to ENE–WSW compression during the Sveconorwegian orogeny (*Mattila and Viola*, 2014) caused the development of low-angle faults in Olkiluoto (*Nordbäck et al.*, 2022, Figure 12B). This faulting event is possibly also observed within the isotopic age data from the PMSZ (*Heeremans and Wijbrans*, 1999, Figure 12A)).

6 Conclusions

In this study, we investigated brittle structures within the 1.58 Ga Åland rapakivi, located within the central parts of Fennoscandia. Based on observations from outcrop-scale fault structures and paleostress analysis, we recognized two separate stages of strike-slip faulting, probably Mesoproterozoic in age. Our results indicate that the first stage of brittle deformation occurred within WNW–ESE to NNW–SSE compression, which caused the formation of E–W-trending dextral strike-slip faults and reactivation of NW–SW-trending Paleoproterozoic shear zones. According to our tentative interpretation, this faulting event occurred around 1.55–1.4 Ga. This stage was followed by a faulting stage within a NE–SW compressional stress regime that caused the less prominent network of N–S dextral and E–W-trending sinistral strike-slip faults, possibly related to dated fault reactivations in Olkiluoto between 1.3–1.2 Ga and the intrusion of post-Jotnian diabase sills. Joint formation in Åland is observed to post-date both faulting stages, but the minimum age of jointing can only be loosely constrained as Precambrian. The above results provide tools to assess the Mesoproterozoic reactivations of Paleoproterozoic shear zones and brittle faults. Based on our regional structural analysis, the emplacement of the Åland rapakivi batholith probably occurred within an E–W to NW–SE extensional setting that caused normal faulting within roughly N–S-trending structures.

Acknowledgements

This study was funded by the Kallioperän rikkonaisuus – Bedrock fracturing project at the Geological Survey of Finland and the KYT KARIKKO project, which is a part of the Finnish Research Programme on Nuclear Waste Management (2019–2022). We are grateful to Stig Abrahamson and the government of Åland for assistance with the planning and logistics of the field work campaigns. Sabina Kraatz (2020) and Kaisa Nikkilä (2020 and 2022), from Åbo Akademi are thanked for their help with field mapping. Constructive comments by editors Laura Federico, Craig Magee and two anonymous reviewers led to a significant improvement of the paper.

Author contributions

Conceptualization: N. Nordbäck, P. Skyttä.
Analysis: N. Nordbäck.
Field work: N. Nordbäck, P. Skyttä, J. Engström, N. Ovaskainen, J. Mattila, I. Aaltonen.
Writing – original draft: N. Nordbäck, P. Skyttä.
Writing – review and editing: J. Engström, N. Ovaskainen, J. Mattila, I. Aaltonen.

Data availability

The lineament source data of southwestern Finland and UAV field data from Geta is presented in the Supporting Information . Fault and joint datasets from Geta are provided as data tables. The Getaberget UAV orthomosaic dataset is available through Zenodo (https://zenodo.org/record/4719627).

Competing interests

The authors declare no competing interests.

Peer review

This publication was peer-reviewed by Maryam Ezati and Nicolas Harrichhausen. The full peer-review report can be found here: tektonika.online/index.php/home/article/view/25/30

Copyright notice

References

Aaltonen, I., K. Front, S. Gehör, and E. Sahlstedt (2018), Hydrothermal Alteration of Bedrock at Olkiluoto, Posiva Report 2018–03, *Tech. rep.*, Posiva Oy, Eurajoki, Finland.

Abdullah, A., S. Nassr, and A. Ghaleeb (2013), Remote sensing and geographic information system for fault segments mapping a study from taiz area, yemen., *Journal of Geological Research*, *2013*, 1–16, doi: 10.1155/2013/201757.

Angelier, J. (1979), Determination of the mean principal directions of stresses for a given fault population, *Tectonophysics*, *56*(3-4), T17–T26, doi: 10.1016/0040-1951(79)90081-7.

Angelier, J. (1984), Tectonic analysis of fault slip data sets, *Journal of Geophysical Research: Solid Earth*, *89*(B7), 5835–5848, doi: 10.1029/JB089iB07p05835.

Angelier, J. (1994), *Continental deformation*, chap. Fault slip analysis and palaeostress reconstruction, pp. 53–100, Pergamon press, Oxford, UK.

Baer, G., M. Beyth, and Z. Reches (1994), Dikes emplaced into fractured basement, timna igneous complex, israel, *Journal of Geophysical Research: Solid Earth*, *99*(B12), 24,039–24,050, doi: 10.1029/94JB02161.

Bai, T., L. Maerten, M. R. Gross, and A. Aydin (2002), Orthogonal cross joints: do they imply a regional stress rotation?, *Journal of structural geology*, *24*(1), 77–88, doi: 10.1016/S0191-8141(01)00050-5.

Bemis, S. P., S. Micklethwaite, D. Turner, M. R. James, S. Akciz, S. T. Thiele, and H. A. Bangash (2014), Ground-based and uav-based photogrammetry: A multi-scale, high-resolution mapping tool for structural geology and paleoseismology, *Journal of structural geology*, *69*, 163–178, doi: 10.1016/j.jsg.2014.10.007.

Bergman, L., R. Tynni, and B. Winterhalter (1982), *Paleozoic sediments in the rapakivi area of the Åland Islands*, vol. 317, 7–34 pp., Geologinen tutkimuslaitos.

Bingen, B., O. Nordgulen, G. Viola, et al. (2008a), A four-phase model for the sveconorwegian orogeny, sw scandinavia, *Norsk geologisk tidsskrift*, *88*(1), 43–72.

Bingen, B., J. Andersson, U. Söderlund, and C. Möller (2008b), The mesoproterozoic in the nordic countries, *Episodes Journal of International Geoscience*, *31*(1), 29–34, doi: 10.18814/epiiugs/2008/v31i1/005.

Bingham, C. (1974), An antipodally symmetric distribution on the sphere, *The Annals of Statistics*, pp. 1201–1225, doi: 10.1214/aos/1176342874.

Blenkinsop, T. G. (2006), Kinematic and dynamic fault slip analyses: implications from the surface rupture of the 1999 chi-chi, taiwan, earthquake, *Journal of Structural Geology*, *28*(6), 1040–1050, doi: 10.1016/j.jsg.2006.03.011.

Bogdanova, S., B. Bingen, R. Gorbatschev, T. Kheraskova, V. Kozlov, V. Puchkov, and Y. A. Volozh (2008), The east european craton (baltica) before and during the assembly of rodinia, *Precambrian Research*, *160*(1-2), 23–45, doi: 10.1016/j.precamres.2007.04.024.

Bott, M. H. P. (1959), The mechanics of oblique slip faulting, *Geological magazine*, *96*(2), 109–117, doi: 10.1017/S0016756800059987.

Branigan, N. (1987), The role of shearing in the proterozoic development of the åland archipelago, sw finland, *Bulletin of the Geological Society of Finland*, *59*, 117–128, doi: 10.17741/BGSF/59.2.005.

Buntin, S., A. Malehmir, H. Koyi, K. Högdahl, M. Malinowski, S. Å. Larsson, H. Thybo, C. Juhlin, A. Korja, and A. Górszczyk (2019), Emplacement and 3d geometry of crustal-scale saucer-shaped intrusions in the fennoscandian shield, *Scientific Reports*, *9*(1), 10,498, doi: 10.1038/s41598-019-46837-x.

Delvaux, D., and B. Sperner (2003), New aspects of tectonic stress inversion with reference to the tensor program, *Geological Society, London, Special Publications*, *212*(1), 75–100, doi: 10.1144/GSL.SP.2003.212.01.0.

Delvaux, D., R. Moeys, G. Stapel, C. Petit, K. Levi, A. Miroshnichenko, V. Ruzhich, and V. San'kov (1997), Paleostress reconstructions and geodynamics of the baikal region, central asia, part 2. cenozoic rifting, *Tectonophysics*, *282*(1-4), 1–38, doi: 10.1016/S0040-1951(97)00210-2.

Dyer, R. (1988), Using joint interactions to estimate paleostress ratios, *Journal of Structural Geology*, *10*(7), 685–699, doi: 10.1016/0191-8141(88)90076-4.

Ehlers, C., and M. Ehlers (1977), Shearing and multiple intrusion in the diabases of aland archipelago, SW Finland.

Ehlers, C., A. Lindroos, and O. Selonen (1993), The late svecofennian granite-migmatite zone of southern finland—a belt of transpressive deformation and granite emplacement, *Precambrian research*, *64*(1-4), 295–309, doi: 10.1016/0301-9268(93)90083-E.

Elminen, T., M.-L. Airo, R. Niemelä, M. Pajunen, M. Vaarma, P. Wasenius, and M. Wennerström (2008), Fault structures in the helsinki area, southern finland, *Geological survey of Finland, Special Paper*, *47*, 185–213.

EMODnet (2018), Emodnet digital bathymetry (dtm 2018), https://doi.org/10.12770/18FF0D48-B203-4A65-94A9-5FD8B0EC35F6, doi: 10.12770/18FF0D48-B203-4A65-94A9-5FD8B0EC35F6.

English, J. M. (2012), Thermomechanical origin of regional fracture systems, *AAPG bulletin*, *96*(9), 1597–1625, doi: 10.1306/01021211018.

Engström, J., A. Kärki, S. Paulamäki, and I. Mänttäri (2022), Palaeoproterozoic structural evolution of polyphase migmatites in olkiluoto, sw finland, *Bulletin of the Geological Society of Finland*, *94*, 119–143, doi: 10.17741/bgsf/94.2.002.

Ezati, M., E. Gholami, and S. M. Mousavi (2020), Paleostress regime reconstruction based on brittle structure analysis in the shekarab mountain, eastern iran, *Arabian Journal of Geosciences*, *13*, 1–18, doi: 10.1007/s12517-020-06235-4.

Friese, N., A. Vollbrecht, B. Leiss, and O. Jacke (2011), Cambrian sedimentary dykes in the proterozoic basement of the västervik area (southeast sweden): episodic formation inferred from macro-and microfabrics, *International Journal of Earth Sciences*, *100*, 741–752, doi: 10.1007/s00531-009-0508-3.

Geological Survey of Finland (2001), Geological map of the fennoscandian shield 1:1 000 000, https://hakku.gtk.fi/en/locations/search.

Geological Survey of Finland (2007a), Aeromagnetic raster data of finland, https://hakku.gtk.fi/en/locations/search.

Geological Survey of Finland (2007b), Aeromagnetic raster data of finland, https://hakku.gtk.fi/en/locations/search.

Gillespie, P., J. Walsh, J. Watterson, C. Bonson, and T. Manzocchi (2001), Scaling relationships of joint and vein arrays from the burren, co. clare, ireland, *Journal of Structural Geology*, *23*(2-3), 183–201, doi: 10.1016/S0191-8141(00)00090-0.

Haapala, I., and O. T. Rämö (1992), Tectonic setting and origin of the proterozoic rapakivi granites of southeastern fennoscandia, *Earth and environmental science transactions of the Royal Society of Edinburgh*, *83*(1-2), 165–171, doi: 10.1017/S0263593300007859.

Hall, A. M., N. Putkinen, S. Hietala, E. Lindsberg, and M. Holma (2021), Ultra-slow cratonic denudation in finland since 1.5 ga indicated by tiered unconformities and impact structures, *Precambrian Research*, *352*, 106,000, doi: 10.1016/j.precamres.2020.106000.

Hardacre, K., and P. Cowie (2003), Variability in fault size scaling due to rock strength heterogeneity: a finite element investigation, *Journal of structural geology*, *25*(10), 1735–1750, doi: 10.1016/S0191-8141(02)00205-5.

Hauta-niemi, H., M. Kurimo, J. Multala, H. Levaniemi, and J. Vironmaki (2005), The" three in one" aerogeophysical concept of gtk in 2004, *Geological survey of Finland, Special Paper*, *39*, 21.

Healy, D., R. R. Jones, and R. E. Holdsworth (2006), Three-dimensional brittle shear fracturing by tensile crack interaction, *Nature*, *439*(7072), 64–67, doi: 10.1038/nature04346.

Heeremans, and Wijbrans (1999), Late proterozoic tectonic events in southern finland, constrained by 40ar/39ar incremental heating and single spot fusion experiments on k-feldspars, *Terra Nova*, *11*(5), 216–222, doi: 10.1046/j.1365-3121.1999.00250.x.

Heeremans, M., H. Stel, P. Van der Beek, and A. Lankreijer (1996), Tectono-magmatic control on vertical dip slip basement faulting: An example from the fennoscandian shield, *Terra Nova*, *8*(2), 129–140, doi: 10.1111/j.1365-3121.1996.tb00737.x.

Hermansson, T., M. B. Stephens, F. Corfu, L. M. Page, and J. Andersson (2008), Migratory tectonic switching, western svecofennian orogen, central sweden: Constraints from u/pb zircon and titanite geochronology, *Precambrian Research*, *161*(3-4), 250–278, doi: 10.1016/j.precamres.2007.08.008.

Hestnes, Å., D. Gasser, T. Scheiber, J. Jacobs, R. van der Lelij, J. Schönenberger, and A. K. Ksienzyk (2022), The brittle evolution of western norway–a space-time model based on fault mineralizations, k–ar fault gouge dating and paleostress analysis, *Journal of Structural Geology*, *160*, 104,621, doi: 10.1016/j.jsg.2022.104621.

Högdahl, K., U. B. Andersson, and O. Eklund (2004), *The Transscandinavian Igneous Belt (TIB) in Sweden: a review of its character and evolution*, vol. 37, Geological survey of Finland Espoo.

Hou, G., M. Santosh, X. Qian, G. S. Lister, and J. Li (2008), Tectonic constraints on 1.3~ 1.2 ga final breakup of columbia supercontinent from a giant radiating dyke swarm, *Gondwana Research*, *14*(3), 561–566, doi: 10.1016/j.gr.2008.03.005.

Jolly, R., and D. Sanderson (1997), A mohr circle construction for the opening of a pre-existing fracture, *Journal of Structural Geology*, *19*(6), 887–892, doi: 10.1016/S0191-8141(97)00014-X.

Kohonen, J., and O. Rämö (2005), Sedimentary rocks, diabases, and late cratonic evolution, *Developments in Precambrian geology*, pp. 563–603, doi: 10.1016/S0166-2635(05)80014-3.

Kohonen, J., P. Pihlaja, H. Kujala, and J. Marmo (1993), Sedimentation of the jotnian satakunta sandstone, western finland, *Bulletin-Geological survey of Finland*, (369).

Korja, A., and P. Heikkinen (1996), Proterozoic extensional tectonics of the central fennoscandian shield: Results from the babel experiment, *GFF*, *118*(S4), 94–94.

Korja, A., T. Korja, U. Luosto, and P. Heikkinen (1993), Seismic and geoelectric evidence for collisional and extensional events in the fennoscandian shield implications for precambrian crustal evolution, *Tectonophysics*, *219*(1-3), 129–152, doi: 10.1016/0040-1951(93)90292-R.

Korja, A., P. Heikkinen, and S. Aaro (2001), Crustal structure of the northern baltic sea palaeorift, *Tectonophysics*, *331*(4), 341–358, doi: 10.1016/S0040-1951(00)00290-0.

Kosunen, P. (1999), The rapakivi granite plutons of bodom and obbnas, southern finland: petrography and geochemistry, *BULLETIN-GEOLOGICAL SOCIETY OF*

FINLAND, *71*(2), 275–304, doi: 10.17741/bgsf/71.2.005.

Kraatz, S. (2013), Airiston hiertovyöhyke - duktiilista deformaatiosta hauraiden rakenteiden ympäristöksi, Master's thesis, Turku University, Turku, Finland.

Kraatz, S. (2022), Analysis of the brittle structural framework of the boxö-vårdö zone, as the northern extension of the south finland shear zone, northeastern åland, Master's thesis, Åbo Akademi University, Turku, Finland, available at https://www.doria.fi/handle/10024/185518.

Krabbendam, M., and T. Bradwell (2014), Quaternary evolution of glaciated gneiss terrains: pre-glacial weathering vs. glacial erosion, *Quaternary Science Reviews*, *95*, 20–42, doi: 10.1016/j.quascirev.2014.03.013.

Lacombe, O. (2012), Do fault slip data inversions actually yield "paleostresses" that can be compared with contemporary stresses? a critical discussion, *Comptes Rendus Geoscience*, *344*(3-4), 159–173, doi: 10.1016/j.crte.2012.01.006.

Lahtinen, R., A. Korja, and M. Nironen (2005), Paleoproterozoic tectonic evolution, *Developments in Precambrian geology*, pp. 481–532, doi: 10.1016/S0166-2635(05)80012-X.

Lahtinen, R., A. Korja, M. Nironen, and P. Heikkinen (2009), Palaeoproterozoic accretionary processes in fennoscandia, *Geological Society, London, Special Publications*, *318*(1), 237–256, doi: 10.1144/SP318.8.

Laitakari, I., T. Rämö, V. Suominen, M. Niin, K. Stepanov, and A. Amantov (1996), Subjotnian: Rapakivi granites and related rocks in the surroundings of the gulf of finland, *Geological survey of Finland, Special Paper*, pp. 59–98.

Larson, Tullborg, Cederbom, and Stiberg (1999), Sveconorwegian and caledonian foreland basins in the baltic shield revealed by fission-track thermochronology, *Terra Nova*, *11*(5), 210–215, doi: 10.1046/j.1365-3121.1999.00249.x.

Li, Z.-X., S. Bogdanova, A. Collins, A. Davidson, B. De Waele, R. Ernst, I. Fitzsimons, R. Fuck, D. Gladkochub, J. Jacobs, et al. (2008), Assembly, configuration, and break-up history of rodinia: a synthesis, *Precambrian research*, *160*(1-2), 179–210, doi: 10.1016/j.precamres.2007.04.021.

Luosto, U., T. Tiira, H. Korhonen, I. Azbel, V. Burmin, A. Buyanov, I. Kosminskaya, V. Ionkis, and N. Sharov (1990), Crust and upper mantle structure along the dss baltic profile in se finland, *Geophysical Journal International*, *101*(1), 89–110, doi: 10.1111/j.1365-246X.1990.tb00760.x.

Maerten, L., P. Gillespie, and D. D. Pollard (2002), Effects of local stress perturbation on secondary fault development, *Journal of Structural Geology*, *24*(1), 145–153, doi: 10.1016/S0191-8141(01)00054-2.

Marchesini, B., P. S. Garofalo, L. Menegon, J. Mattila, and G. Viola (2019), Fluid-mediated, brittle–ductile deformation at seismogenic depth–part 1: Fluid record and deformation history of fault veins in a nuclear waste repository (olkiluoto island, finland), *Solid Earth*, *10*(3), 809–838, doi: 10.5194/se-10-809-2019.

Marrett, R., and R. W. Allmendinger (1990), Kinematic analysis of fault-slip data, *Journal of structural geology*, *12*(8), 973–986, doi: 10.1016/0191-8141(90)90093-E.

Marrett, R., and D. C. Peacock (1999), Strain and stress, *Journal of structural geology*, *21*(8-9), 1057–1063, doi: 10.1016/S0191-8141(99)00020-6.

Mattila, J., and G. Viola (2014), New constraints on 1.7 gyr of brittle tectonic evolution in southwestern finland derived from a structural study at the site of a potential nuclear waste repository (olkiluoto island), *Journal of Structural Geology*, *67*, 50–74, doi: 10.1016/j.jsg.2014.07.003.

McKeagney, C., C. Boulter, R. Jolly, and R. Foster (2004), 3-d mohr circle analysis of vein opening, indarama lode-gold deposit, zimbabwe: implications for exploration, *Journal of Structural Geology*, *26*(6), 1275–1291, doi: 10.1016/j.jsg.2003.11.001.

Morris, A., D. A. Ferrill, and D. Henderson (1996), Slip-tendency analysis and fault reactivation, *Geology*, *24*(3), 275–278, doi: 10.1130/0091-7613(1996)024<0275:STAAFR>2.3.CO;2.

Munier, R., and C. J. Talbot (1993), Segmentation, fragmentation and jostling of cratonic basement in and near Äspö, southeast sweden, *Tectonics*, *12*(3), 713–727, doi: 10.1029/92TC02722.

Nadan, B. J., and T. Engelder (2009), Microcracks in New England granitoids: A record of thermoelastic relaxation during exhumation of intracontinental crust, *GSA Bulletin*, *121*(1-2), 80–99, doi: 10.1130/B26202.1.

National Land Survey of Finland (2019), Laser scanning 2008-2019 by national land survey of finland, https://www.maanmittauslaitos.fi/en/maps-and-spatial-data/expert-users/product-descriptions/laser-scanning-data.

Nironen, M. (1997), The svecofennian orogen: a tectonic model, *Precambrian Research*, *86*(1), 21–44, doi: 10.1016/S0301-9268(97)00039-9.

Nordbäck, N., and N. Ovaskainen (2022), Getaberget drone orthomosaic dataset, doi: 10.5281/ZENODO.4719627.

Nordbäck, N., J. Mattila, H. Zwingmann, and G. Viola (2022), Precambrian fault reactivation revealed by structural and k-ar geochronological data from the spent nuclear fuel repository in olkiluoto, southwestern finland, *Tectonophysics*, *824*, 229,208, doi: 10.1016/j.tecto.2022.229208.

Nordbäck, N., N. Ovaskainen, M. Markovaara-Koivisto, P. Skyttä, A. Ojala, J. Engström, and C. Nixon (2023), Multiscale mapping and scaling analysis of the censored brittle structural framework within the crystalline bedrock of southern finland., *Bulletin of the Geological Society of Finland*, *95*(1), doi: 10.17741/bgsf/95.1.001.

Nyberg, B., C. W. Nixon, and D. J. Sanderson (2018), Networkgt: A gis tool for geometric and topological analysis of two-dimensional fracture networks, *Geosphere*, *14*(4), 1618–1634, doi: 10.1130/GES01595.1.

O'Leary, D. W., J. D. Friedman, and H. A. Pohn (1976), Lineament, linear, lineation: Some proposed new standards for old terms, *GSA Bulletin*, *87*(10), 1463–1469, doi: 10.1130/0016-7606(1976)87<1463:LLLSPN>2.0.CO;2.

Ovaskainen, N., N. Nordbäck, P. Skyttä, and J. Engström (2022), A new subsampling methodology to optimize the characterization of two-dimensional bedrock fracture networks, *Journal of Structural Geology*, *155*, 104,528, doi: 10.1016/j.jsg.2022.104528.

Ovaskainen, N., P. Skyttä, N. Nordbäck, and J. Engström (2023), Detailed investigation of multi-scale fracture networks in glacially abraded crystalline bedrock at Åland islands, finland, *Solid Earth*, *14*(6), 603–624, doi: 10.5194/se-14-603-2023.

Pajunen, M., M.-L. Airo, T. Elminen, I. Mänttäri, R. Niemelä, M. Vaarma, P. Wasenius, and M. Wennerström (2008),

Tectonic evolution of the svecofennian crust in southern finland, *Geological Survey of Finland, Special Paper*, *47*, 15–160.

Parfrey, L. W., D. J. G. Lahr, A. H. Knoll, and L. A. Katz (2011), Estimating the timing of early eukaryotic diversification with multigene molecular clocks, *Proceedings of the National Academy of Sciences*, *108*(33), 13,624–13,629, doi: 10.1073/pnas.1110633108.

Pascal, C. (2021), *Paleostress inversion techniques: methods and applications for tectonics*, Elsevier.

Peacock, D., D. Sanderson, and A. Rotevatn (2018), Relationships between fractures, *Journal of Structural Geology*, *106*, 41–53, doi: 10.1016/j.jsg.2017.11.010.

Peacock, D. C. P., C. Nixon, A. Rotevatn, D. Sanderson, and L. Zuluaga (2016), Glossary of fault and other fracture networks, *Journal of Structural Geology*, *92*, 12–29, doi: 10.1016/j.jsg.2016.09.008.

Pitkälä, I. (2019), Shear zones and structural analysis of the loimaa area, sw finland, Master's thesis, University of Turku, Turku, Finland, available at https://urn.fi/URN:NBN:fi-fe2019090627211.

Pokki, J., J. Kohonen, R. Lahtinen, O. Rämö, and T. Andersen (2013), *Petrology and Provenance of the Mesoproterozoic Satakunta Formation, SW Finland*, Tutkimusraportti, Geological Survey of Finland.

Pollard, D. D. (1987), Theoretical displacements and stresses near fractures in rock: with applications to faults, joints, veins, dikes, and solution surfaces, *Fracture mechanics of rock*, pp. 277–349, doi: 10.1016/B978-0-12-066266-1.50013-2.

Pollard, D. D., and A. Aydin (1988), Progress in understanding jointing over the past century, *Geological Society of America Bulletin*, *100*(8), 1181–1204, doi: 10.1130/0016-7606(1988)100<1181:PIUJOT>2.3.CO;2.

Prando, F., L. Menegon, M. Anderson, B. Marchesini, J. Mattila, and G. Viola (2020), Fluid-mediated, brittle–ductile deformation at seismogenic depth–part 2: stress history and fluid pressure variations in a shear zone in a nuclear waste repository (olkiluoto island, finland), *Solid Earth*, *11*(2), 489–511, doi: 10.5194/se-11-489-2020.

Rasmussen, B., J. R. Muhling, J.-W. Zi, H. Tsikos, and W. W. Fischer (2020), A 1.25 ga depositional age for the "paleoproterozoic" mapedi red beds, kalahari manganese field, south africa: New constraints on the timing of oxidative weathering and hematite mineralization, *Geology*, *48*(1), 44–48, doi: 10.1130/G46707.1.

Riller, U., M. Clark, H. Daxberger, D. Doman, I. Lenauer, S. Plath, and T. Santimano (2017), Fault-slip inversions: Their importance in terms of strain, heterogeneity, and kinematics of brittle deformation, *Journal of Structural Geology*, *101*, 80–95, doi: 10.1016/j.jsg.2017.06.013.

Roberts, N. M. (2013), The boring billion?–lid tectonics, continental growth and environmental change associated with the columbia supercontinent, *Geoscience Frontiers*, *4*(6), 681–691, doi: 10.1016/j.gsf.2013.05.004.

Rämö, O., and I. Haapala (1995), One hundred years of rapakivi granite, *Mineralogy and Petrology*, *52*, 129–185, doi: 10.1007/BF01163243.

Rämö, O., and I. Haapala (2005), Chapter 12 rapakivi granites, in *Precambrian Geology of Finland Key to the Evolution of the Fennoscandian Shield*, *Developments in Precambrian Geology*, vol. 14, edited by M. Lehtinen, P. Nurmi, and O. Ramö, pp. 533–562, Elsevier, doi: 10.1016/S0166-2635(05)80013-1.

Saintot, A., M. Stephens, G. Viola, and Ø. Nordgulen (2011), Brittle tectonic evolution and paleostress field reconstruction in the southwestern part of the fennoscandian shield, forsmark, sweden, *Tectonics*, *30*(4), doi: 10.1029/2010TC002781.

Salminen, P. E., P. Hölttä, R. Lahtinen, and M. Sayab (2022), Monazite record for the paleoproterozoic svecofennian orogeny, se finland: An over 150-ma spread of monazite dates, *Lithos*, *416*, 106,654, doi: 10.1016/j.lithos.2022.106654.

Scheiber, T., and G. Viola (2018), Complex bedrock fracture patterns: A multipronged approach to resolve their evolution in space and time, *Tectonics*, *37*(4), 1030–1062, doi: 10.1002/2017TC004763.

Scholz, C. (2007), Fault mechanics, *Crust and Lithosphere Dynamics*, *6*, 441–483, doi: 10.1016/B978-0-444-53802-4.00119-6.

Sibson, R. (1977), Fault rocks and fault mechanisms, *Journal of the Geological Society*, *133*(3), 191–213, doi: 10.1144/gsjgs.133.3.0191.

Sibson, R. H. (1981), Fluid flow accompanying faulting: field evidence and models, *Earthquake prediction: an international review*, *4*, 593–603, doi: 10.1029/ME004p0593.

Sjöström, H., and K. S. Persson (2001), Deformation zones in eastern bergslagen (uppland-sörmland).

Skyttä, P., J. Kinnunen, J.-P. Palmu, and K. Korkka-Niemi (2015), Bedrock structures controlling the spatial occurrence and geometry of 1.8 ga younger glacifluvial deposits—example from first salpausselkä, southern finland, *Global and Planetary Change*, *135*, 66–82, doi: 10.1016/j.gloplacha.2015.10.007.

Skyttä, P., N. Ovaskainen, N. Nordbäck, J. Engström, and J. Mattila (2021), Fault-induced mechanical anisotropy and its effects on fracture patterns in crystalline rocks, *Journal of Structural Geology*, *146*, 104,304, doi: 10.1016/j.jsg.2021.104304.

Skyttä, P., N. Nordbäck, A. Ojala, N. Putkinen, I. Aaltonen, J. Engström, J. Mattila, and N. Ovaskainen (2023), The interplay of bedrock fractures and glacial erosion in defining the present-day land surface topography in mesoscopically isotropic crystalline rocks, *Earth Surface Processes and Landforms*, doi: 10.1002/esp.5596.

Soesoo, A., V. Puura, J. Kirs, V. Petersell, M. Niin, and T. All (2004), Outlines of the precambrian basement of estonia, in *Proceedings of the Estonian Academy of Sciences, Geology*, vol. 53, pp. 149–164.

Soliman, A., and L. Han (2019), Effects of vertical accuracy of digital elevation model (dem) data on automatic lineaments extraction from shaded dem, *Advances in space research*, *64*(3), 603–622, doi: 10.1016/j.asr.2019.05.009.

Sornette, A., P. Davy, and D. Sornette (1993), Fault growth in brittle-ductile experiments and the mechanics of continental collisions, *Journal of Geophysical Research: Solid Earth*, *98*(B7), 12,111–12,139, doi: 10.1029/92JB01740.

Sperner, B., and P. Zweigel (2010), A plea for more caution in fault–slip analysis, *Tectonophysics*, *482*(1-4), 29–41, doi: 10.1016/j.tecto.2009.07.019.

Stephens, M. B., and S. Bergman (2020), Chapter 2 regional

context and lithotectonic framework of the 2.0–1.8 ga svecokarelian orogen, eastern sweden, *Geological Society, London, Memoirs*, *50*(1), 19–26, doi: 10.1144/M50-2017-2.

Suominen, V. (1991), The chronostratigraphy of southwestern finland with special reference to postjotnian and subjotnian diabases, *Bulletin-Geological Survey of Finland*, (356).

Tartaglia, G., G. Viola, A. Ceccato, S. Bernasconi, R. van der Lelij, and T. Scheiber (2020), Multiphase brittle tectonic evolution of the mid-norwegian margin, central norway, reconstructed by remote sensing, paleostress inversion and k-ar fault rock dating, in *EGU General Assembly Conference Abstracts*, p. 5438, doi: 10.5194/egusphere-egu2020-5438.

Tillberg, M., H. Drake, T. Zack, E. Kooijman, M. J. Whitehouse, and M. E. Åström (2020), In situ rb-sr dating of slickenfibres in deep crystalline basement faults, *Scientific reports*, *10*(1), 562, doi: 10.1038/s41598-019-57262-5.

Tillberg, M., H. Drake, T. Zack, J. Hogmalm, E. Kooijman, and M. Åström (2021), Reconstructing craton-scale tectonic events via in situ rb-sr geochronology of poly-phased vein mineralization, *Terra Nova*, *33*(5), 502–510, doi: 10.1111/ter.12542.

Torvela, T., and C. Ehlers (2010), From ductile to brittle deformation: structural development and strain distribution along a crustal-scale shear zone in sw finland, *International Journal of Earth Sciences*, *99*, 1133–1152, doi: 10.1007/s00531-009-0451-3.

Torvela, T., and M. Kurhila (2020), How does orogenic crust deform? evidence of crustal-scale competent behaviour within the partially molten middle crust during orogenic compression, *Precambrian Research*, *342*, 105,670, doi: 10.1016/j.precamres.2020.105670.

Torvela, T., I. Mänttäri, and T. Hermansson (2008), Timing of deformation phases within the south finland shear zone, sw finland, *Precambrian Research*, *160*(3-4), 277–298, doi: 10.1016/j.precamres.2007.08.002.

Tynni, R. (1982), On paleozoic microfossils in clastic dykes in the aland islands and in the core samples of lumparn. in: Paleozoic sediments in the rapakivi area of the aland islands, *Bulletin of the Geological Society of Finland*.

Vaasjoki, M. (1977), Rapakivi granites and other postorogenic rocks in finland: their age and the lead isotopic composition of certain associated galena mineralizations, *Geol. Surv. Finl., Bull.;(Finland)*, *294*.

Vaasjoki, M. (1996), *Explanation to the geochronological map of southern Finland: The development of the continental crust with special reference to the Svecofennian orogeny*, vol. 135, Geological Survey of Finland.

Väisänen, M., and P. Hölttä (1999), Structural and metamorphic evolution of the turku migmatite complex, southwestern finland, *Bulletin of the Geological Society of Finland*, *71*(1), 177–218.

Väisänen, M., and P. Skyttä (2007), Late svecofennian shear zones in southwestern finland, *Gff*, *129*(1), 55–64, doi: 10.1080/11035890701291055.

Van Balen, R., and M. Heeremans (1998), Middle proterozoic–early palaeozoic evolution of central baltoscandian intracratonic basins: evidence for asthenospheric diapirs, *Tectonophysics*, *300*(1-4), 131–142, doi: 10.1016/S0040-1951(98)00237-6.

Vigneresse, J. L. (2005), The specific case of the mid-proterozoic rapakivi granites and associated suite within the context of the columbia supercontinent, *Precambrian research*, *137*(1-2), 1–34, doi: 10.1016/j.precamres.2005.01.001.

Viola, G., G. Venvik Ganerød, and C.-H. Wahlgren (2009), Unraveling 1.5 ga of brittle deformation history in the laxemar-simpevarp area, southeast sweden: A contribution to the swedish site investigation study for the disposal of highly radioactive nuclear waste, *Tectonics*, *28*(5), doi: 10.1029/2009TC002461.

Viola, G., I. Henderson, B. Bingen, and B. Hendriks (2011), The grenvillian–sveconorwegian orogeny in fennoscandia: back-thrusting and extensional shearing along the "mylonite zone", *Precambrian Research*, *189*(3-4), 368–388, doi: 10.1016/j.precamres.2011.06.005.

Viola, G., A. Kounov, M. Andreoli, and J. Mattila (2012), Brittle tectonic evolution along the western margin of south africa: more than 500 myr of continued reactivation, *Tectonophysics*, *514*, 93–114, doi: 10.1016/j.tecto.2011.10.009.

Viola, G., H. Zwingmann, J. Mattila, and A. Käpyaho (2013), K-ar illite age constraints on the proterozoic formation and reactivation history of a brittle fault in fennoscandia, *Terra Nova*, *25*(3), 236–244, doi: 10.1111/ter.12031.

Wallace, R. E. (1951), Geometry of shearing stress and relation to faulting, *The Journal of geology*, *59*(2), 118–130, doi: 10.1086/625831.

Yamaji, A. (2016), Genetic algorithm for fitting a mixed bingham distribution to 3d orientations: a tool for the statistical and paleostress analyses of fracture orientations, *Island Arc*, *25*(1), 72–83, doi: 10.1111/iar.12135.

Yamaji, A., K. Sato, and S. Tonai (2010), Stochastic modeling for the stress inversion of vein orientations: Paleostress analysis of pliocene epithermal veins in southwestern kyushu, japan, *Journal of Structural Geology*, *32*(8), 1137–1146, doi: 10.1016/j.jsg.2010.07.001.

Zhao, G., P. A. Cawood, S. A. Wilde, and M. Sun (2002), Review of global 2.1–1.8 ga orogens: implications for a pre-rodinia supercontinent, *Earth-Science Reviews*, *59*(1), 125–162, doi: 10.1016/S0012-8252(02)00073-9.

Žalohar, J., and M. Vrabec (2007), Paleostress analysis of heterogeneous fault-slip data: The gauss method, *Journal of Structural Geology*, *29*(11), 1798–1810, doi: 10.1016/j.jsg.2007.06.009.